Cell Metabolism

Resource

FALCON systematically interrogates free fatty acid biology and identifies a novel mediator of lipotoxicity

Graphical abstract

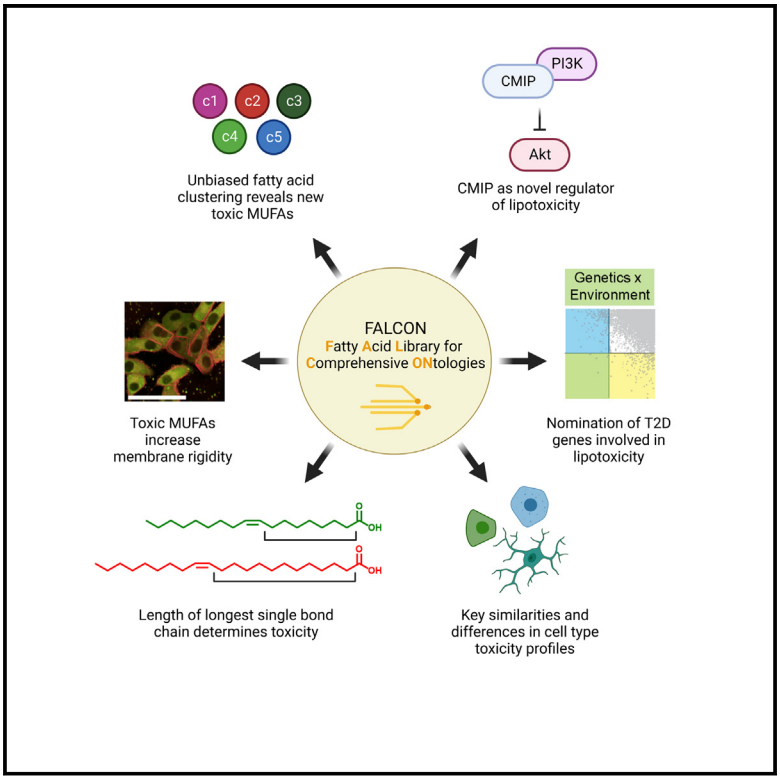

Authors

Nicolas Wieder, Juliana Coraor Fried, Choah Kim, ..., Jillian L. Shaw, Juan Lorenzo Pablo, Anna Greka

Correspondence

agreka@bwh.harvard.edu

In brief

Wieder and Coraor Fried et al. designed fatty acid library for comprehensive ontologies (FALCON) to systematically profile the effects of diverse free fatty acids (FFAs) on different cell types. Unbiased grouping of FFAs revealed a novel subset of toxic monounsaturated FFAs, and integration with human genomic data revealed lipotoxicity regulators.

Highlights

- Fatty acid library for comprehensive ontologies (FALCON) profiles diverse fatty acids
- FALCON's unbiased grouping of fatty acids (FFAs) is applicable to multiple cell types
- Lipotoxic FFAs include monounsaturated fatty acids that decrease membrane fluidity
- FALCON identifies CMIP at the intersection of environmental and genetic disease risk

Wieder et al., 2023, Cell Metabolism *35*, 887–905
May 2, 2023
https://doi.org/10.1016/j.cmet.2023.03.018

CellPress

Cell Metabolism

CellPress
OPEN ACCESS

Resource

FALCON systematically interrogates free fatty acid biology and identifies a novel mediator of lipotoxicity

Nicolas Wieder,[1,2,3,4,18] Juliana Coraor Fried,[1,2,3,18] Choah Kim,[1,2,3] Eriene-Heidi Sidhom,[1,2,3] Matthew R. Brown,[1] Jamie L. Marshall,[1] Carlos Arevalo,[1] Moran Dvela-Levitt,[1,2,3,5] Maria Kost-Alimova,[1] Jonas Sieber,[6] Katlyn R. Gabriel,[1] Julian Pacheco,[1] Clary Clish,[1] Hamdah Shafqat Abbasi,[1] Shantanu Singh,[1] Justine C. Rutter,[1,3] Martine Therrien,[1] Haejin Yoon,[7,8] Zon Weng Lai,[9] Aaron Baublis,[9] Renuka Subramanian,[10] Ranjan Devkota,[1,11] Jonnell Small,[1,3,11] Vedagopuram Sreekanth,[1,12] Myeonghoon Han,[1] Donghyun Lim,[1] Anne E. Carpenter,[1] Jason Flannick,[1,3,13] Hilary Finucane,[1,14] Marcia C. Haigis,[1,7,8] Melina Claussnitzer,[1,3,15] Eric Sheu,[10] Beth Stevens,[1,3,16,17] Bridget K. Wagner,[1,11] Amit Choudhary,[1,3,11,12] Jillian L. Shaw,[1] Juan Lorenzo Pablo,[1] and Anna Greka[1,2,3,19,*]

[1]Broad Institute of MIT and Harvard, Cambridge, MA 02142, USA
[2]Department of Medicine, Brigham and Women's Hospital, Boston, MA 02115, USA
[3]Harvard Medical School, Boston, MA 02115, USA
[4]Department of Neurology with Experimental Neurology and Berlin Institute of Health, Charité, 10117 Berlin, Germany
[5]The Mina and Everard Goodman Faculty of Life Sciences, Bar-Ilan University, Ramat-Gan, Israel
[6]Department of Endocrinology, Metabolism and Cardiovascular Systems, University of Fribourg, Fribourg, Switzerland
[7]Department of Cell Biology, Blavatnik Institute, Harvard Medical School, Boston, MA 02115, USA
[8]Ludwig Center for Cancer Research at Harvard, Boston, MA 02115, USA
[9]Harvard Chan Advanced Multiomics Platform, Harvard T.H. Chan School of Public Health, Boston, MA 02115, USA
[10]Laboratory for Surgical and Metabolic Research, Brigham and Women's Hospital, Harvard Medical School, Boston, MA 02115, USA
[11]Chemical Biology and Therapeutics Science, Broad Institute of MIT and Harvard, Cambridge, MA 02142, USA
[12]Divisions of Renal Medicine and Engineering, Brigham and Women's Hospital, Boston, MA 02115, USA
[13]Division of Genetics and Genomics, Boston Children's Hospital, Boston, MA 02115, USA
[14]Analytic and Translational Genetics Unit, Mass General Hospital, Boston, MA 02114, USA
[15]Metabolism Program, Broad Institute of MIT and Harvard, Cambridge, MA 02142, USA
[16]Boston Children's Hospital, F.M. Kirby Neurobiology Center, Boston, MA 02115, USA
[17]Howard Hughes Medical Institute, Boston, MA 02115, USA
[18]These authors contributed equally
[19]Lead contact
*Correspondence: agreka@bwh.harvard.edu
https://doi.org/10.1016/j.cmet.2023.03.018

SUMMARY

Cellular exposure to free fatty acids (FFAs) is implicated in the pathogenesis of obesity-associated diseases. However, there are no scalable approaches to comprehensively assess the diverse FFAs circulating in human plasma. Furthermore, assessing how FFA-mediated processes interact with genetic risk for disease remains elusive. Here, we report the design and implementation of fatty acid library for comprehensive ontologies (FALCON), an unbiased, scalable, and multimodal interrogation of 61 structurally diverse FFAs. We identified a subset of lipotoxic monounsaturated fatty acids associated with decreased membrane fluidity. Furthermore, we prioritized genes that reflect the combined effects of harmful FFA exposure and genetic risk for type 2 diabetes (T2D). We found that c-MAF-inducing protein (CMIP) protects cells from FFA exposure by modulating Akt signaling. In sum, FALCON empowers the study of fundamental FFA biology and offers an integrative approach to identify much needed targets for diverse diseases associated with disordered FFA metabolism.

INTRODUCTION

Cellular models of fatty acid overload have been used to define "lipotoxicity" as the harmful effects of prolonged and increased exposure to specific lipids,[1,2] but the link between cellular exposure to diverse fatty acid species and toxicity phenotypes remains poorly understood. Not all fatty acids produce the same cellular effects, and distinctions are often made based on their saturation level. Saturated fatty acids (SFAs) contain no double bonds in their carbon chains. In contrast, monounsaturated fatty acids (MUFAs) contain one double bond and polyunsaturated fatty acids (PUFAs) contain more than one double bond. At the cellular level, studies to date have primarily relied on the effects of a single SFA, palmitic acid (PA),[3,4] to explore the role of free

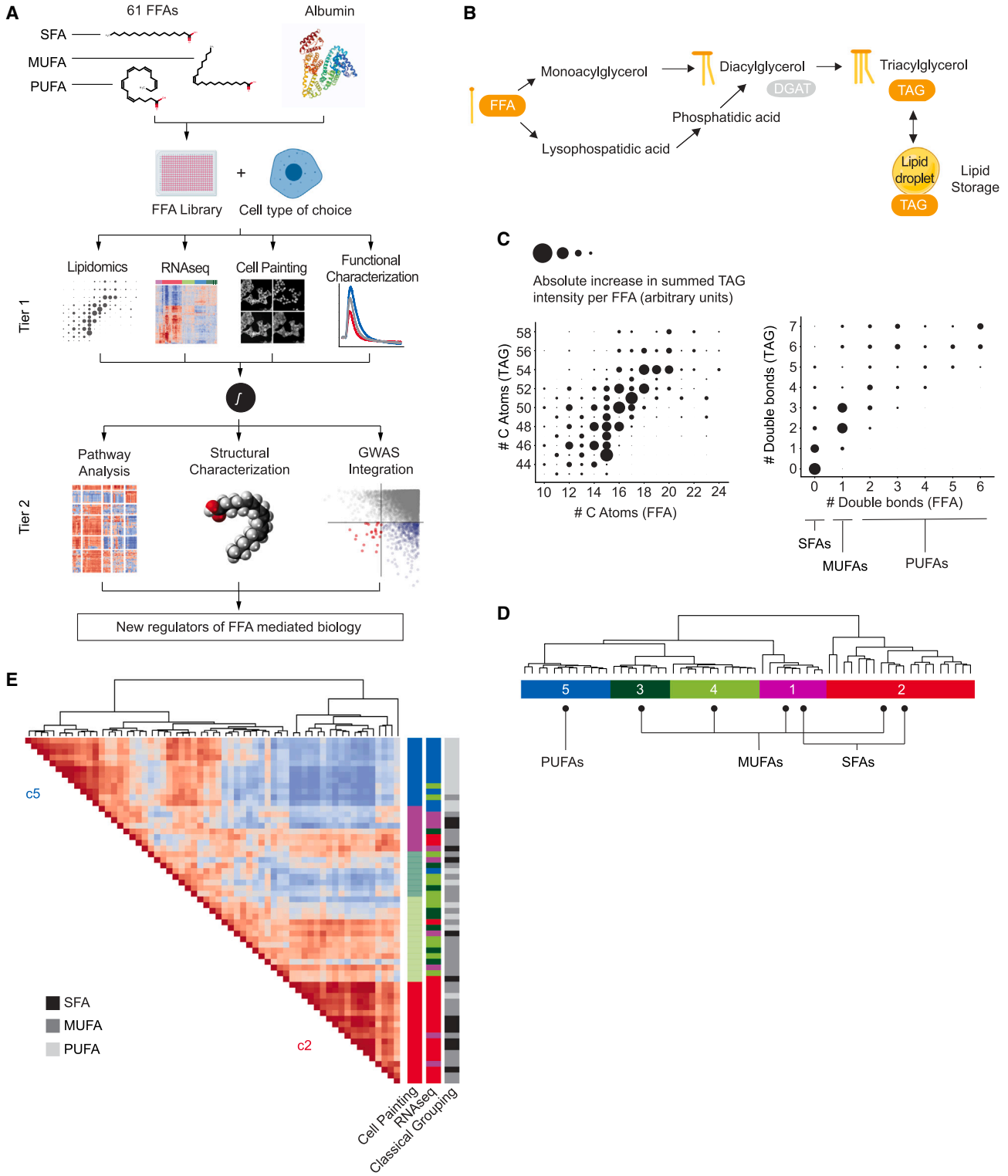

Figure 1. FALCON, a multiplexed platform for the systematic interrogation of structurally diverse FFAs, defines 5 FFA clusters

(A) Analysis workflow for FALCON.

(B) Schematic of triacylglyceride (TAG) synthesis from FFAs. Shown here are the monoacylglycerol (top) and the glycerol-3-phosphate pathway (bottom). For simplicity, the acylation of dihydroxyacetone phosphate is not shown.

(legend continued on next page)

fatty acids (FFAs) in lipotoxicity. However, large-scale epidemiological studies, including the Framingham Heart Study, have shown an association between the abundance of triacylglyceride (TAG) species composed of a wide spectrum of structurally diverse FFAs and the severity of metabolic diseases,[5] hinting at the importance of largely unexplored and clinically relevant FFA biology. Considering that (1) TAGs are hydrolyzed by lipases into FFAs (and glycerol) before uptake into peripheral cells[6] and (2) there is a strong association between TAG composition and obesity-associated diseases such as type 2 diabetes (T2D),[5,7] there is an urgent need to interrogate the biological effects of FFAs across their structural spectrum.

Here, we reveal fatty acid library for comprehensive ontologies (FALCON), a cell-based platform for the unbiased, multimodal investigation of structurally diverse FFAs found in human plasma[8–10] by integrating transcriptomics, cell morphological features, lipidomics, FFA structural characterization, and functional profiling. Out of 61 FFAs, FALCON identified 20 FFAs that were toxic to β cells, grouped into a cluster marked by a distinct transcriptomic signature. These lipotoxic FFAs could not be classified based on degree of saturation alone. More than half (12/20) were MUFAs whose toxicity is not fully understood on a mechanistic level. Exposure to these MUFAs was associated with a distinct lipidomic profile and decreased membrane fluidity. Aiming to understand the combined effects of environmental exposure and genetic risk for T2D, we prioritized 25 genes that emerged from the overlap between genes differentially regulated after exposure to lipotoxic FFAs and genes nominated in a large-scale T2D GWAS. We thus identified *CMIP*, a gene with no prior mechanistic links to metabolic disease, and showed that it protects mouse and human pancreatic β cells from excess fatty acid exposure. In sum, FALCON empowered a comprehensive, multiplexed query of FFA biology and revealed c-MAF-inducing protein (CMIP) as a previously unrecognized suppressor of lipotoxicity.

RESULTS

A systematic approach to study FFA biology

While liver, adipose, and muscle cells play a central role in insulin resistance,[11] T2D GWAS to date have highlighted genes critical to β cell function.[12–15] *In vitro*, β cells are strongly affected by lipid overload; excess chronic fatty acid exposure disrupts their metabolic homeostasis and insulin secretion capacity, pushing them toward ER stress and cell death.[16,17] We developed FALCON with MIN6 cells, a widely used mouse insulinoma pancreatic β cell line that displays robust glucose-sensing and insulin secretion and shares well-conserved molecular programs with human β cells.[18,19]

FALCON (1) curates a comprehensive set of FFAs (Table S1) beyond those traditionally used in targeted experiments (mostly PA and oleic acid [OA]), (2) engineers an approach that solves the difficulty of working with compounds of varying levels of hydrophobicity, and (3) assesses the biological effects of these FFAs in an unbiased fashion. Most of the analyzed FFAs were readily detectable in both human and mouse blood (Table S1).

We generated several datasets to deeply phenotype the effects of treating cells with each of the 61 FFAs including measures of cell viability/function, lipidomics, transcriptomics, and cell morphology (Figure 1A, tier 1). We analyzed and integrated these diverse datasets using (1) gene set enrichment analysis (GSEA[20]) to identify alterations in cellular pathway activity, (2) molecular operating environment (MOE) software[21] to correlate FFA chemical structures with biological features, and (3) multimarker analysis of genomic annotation (MAGMA[22]) ranking to incorporate genetic predisposition to human metabolic disease (Figure 1A, tier 2). Importantly, we validated our results from MIN6 cells in two human β cell systems: iPSC-derived pancreatic β cells and acutely isolated human pancreatic islets from donors. Collectively, this multimodal approach allowed us to (1) group FFAs in an unbiased manner (i.e., remaining agnostic to structural features) solely based on similarity of biological readouts, (2) identify previously unrecognized lipotoxic FFAs, and (3) define toxicity phenotypes representative of these lipotoxic FFAs.

The crucial gating step in establishing FALCON was the ability to reproducibly and reliably deliver solvent-free bovine serum albumin (BSA)-bound FFAs to cells in multiwell plates at scale, using concentrations of magnitude similar to human blood.[8,9,23–28] To achieve this goal, we generated solvent-free crystals of BSA-bound FFAs (Figures S1A and S1B). The crystals were dissolved in culture medium, which was then applied to cells (Figure S1A).

To assess the effects of FFA treatment on cellular lipid composition, we performed mass spectrometry-based lipidomics of cells exposed to each of the 61 FFAs (Figure S1C). TAGs, which are synthesized from FFAs available within a cell[29] (Figure 1B), constituted the majority of detected lipid species. FFAs were likely incorporated into cellular TAGs, as evidenced by the correlation between FFA and TAG structural features, such as chain length and number of double bonds (Figures 1C and S1D).

Identification of non-canonical FFA clusters

To comprehensively define FFA-induced cell states without prior assumptions about biological effects or FFA structural features, we generated transcriptomic profiles of MIN6 cells in response to each of 61 FFAs in the library (Figure S1E). We detected induction of carnitine palmitoyltransferase 1 expression (CPT1A), the rate-limiting enzyme of FFA β-oxidation,[30] across the entire library, demonstrating successful FFA delivery and intracellular metabolism (Figure S1F). Hierarchical clustering of FFA-induced transcriptomes revealed 5 distinct "clusters" (c1–c5) (Figures 1D, S2A, and S2B). At the extremes, FFAs segregated by saturation and chain length: SFAs were major constituents of cluster 1 (c1) and also well represented in cluster 2 (c2; 8/20 c2 FFAs were SFAs), whereas cluster 5 (c5) was exclusively composed of PUFAs. In line with the traditional

(C) Qualitative correlation of structural features (number of C atoms, number of double bonds) of externally applied FFAs from the library (x axis) versus structural features of endogenous TAGs (y axis) measured by lipidomics. Distinct TAG profiles were detected in cells treated with SFAs, MUFAs, or PUFAs.
(D) Five FFA clusters (c1–c5) were identified after hierarchical clustering of transcriptomic profiles derived from exposure to each of 61 FFAs (STAR Methods).
(E) Cell Painting analysis of immunofluorescence images from cells exposed to each of 61 FFAs (STAR Methods) independently clustered together the FFAs transcriptomically assigned to c2 and separately the FFAs assigned to c5.

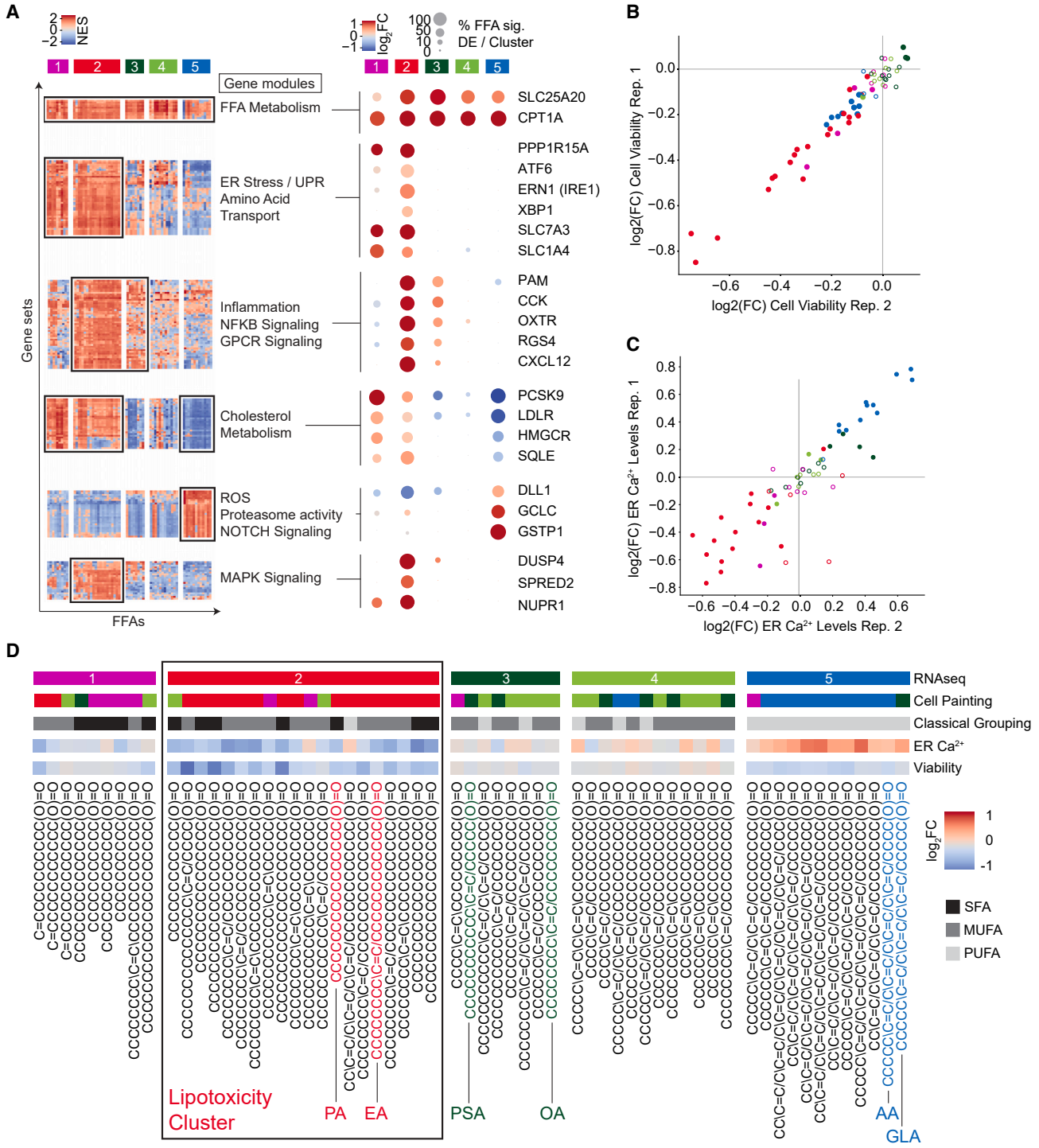

Figure 2. Transcriptomic analysis identifies key biological responses to FFAs, and functional assays validate novel FFA clustering

(A) Hierarchical clustering of a gene set enrichment matrix (based on normalized enrichment scores of gene sets, NES) revealed gene set modules of interest. Representative leading edge genes from each module are listed on the right.

(B and C) Scatterplots of two independent replicates of cell viability (B) and ER Ca^{2+} level measurements (C) (n = 5–7 replicates/FFA/screen). Closed dots represent FFAs that showed significant difference ($p < 0.05$, Bonferroni) from controls in both replicates; open dots represent non-significant FFAs in at least one replicate. Colors indicate corresponding FFA cluster membership (Figure 1D).

(legend continued on next page)

paradigm,[3] PA (lipotoxic FFA) and OA (lipotoxicity-protective FFA) clustered separately, in c2 and c3, respectively. MUFAs were distributed across four clusters c1 to c4 (Figure 1D), indicating that the transcriptomic signatures classified some MUFAs as functionally similar to SFAs, and not to other MUFAs. Of note, traditional criteria (SFA, MUFA, and PUFA)[3] do not adequately capture the observed transcriptomically defined heterogeneity (Figure S2C).

To probe cellular responses to FFA exposure using an independent method, we profiled the entire FFA library using Cell Painting, a high-content image analysis method that simultaneously measures several hundred cellular imaging features[31] (Figure S2D). This morphologic analysis independently clustered together the SFAs and MUFAs transcriptomically assigned to c2 and separated them from the PUFAs in c5 (Figure 1E). Thus, the algorithms analyzing the cell imaging data were in agreement with the FFA clustering derived from transcriptomics with regard to the two most prominent clusters: c2 and c5 (Figures 1D and 1E).

Cellular transcriptomes define key biological responses to FFAs

To understand the basis behind the FFA clusters identified by FALCON, we applied GSEA[20] to each of the 61 FFA-induced transcriptomes using multiple gene set collections (MSigDB[32]). We were able to categorize gene sets across the 5 clusters into modules of gene expression (Figure 2A; STAR Methods). This analysis ensured that our gene set annotation was comprehensive and not reliant on any single database of curated gene lists.

Consistent with exposure of cells to FFAs, a key module shared among all clusters represented pathways regulating FFA transport and metabolism including upregulation of core genes that encode the mitochondrial carnitine shuttle.[33,34] A second module, whose induction (positive normalized enrichment score [NES]) was detected specifically in c1 and c2, consisted of ER stress and unfolded protein response (UPR) genes[35] (Figure 2A). A third gene module comprised stress response pathways, NF-κB signaling, and inflammation (Figure 2A) consistent with lipotoxicity.[36–38] Genes in the third module were specifically upregulated in the c2 FFA cluster. Module four comprised pathways related to cholesterol metabolism,[39–41] and module five consisted of programs related to proteasome activity and responses to reactive oxygen species (ROS) (Figure 2A). A sixth gene module was associated with MAPK signaling, a crucial regulator of cell proliferation, apoptosis, and insulin secretion in β cells.[42] The MAPK signaling module was specifically upregulated in the c2 cluster (Figure 2A). In sum, FALCON defined the biological processes that served as the basis for the separation of diverse FFAs into five previously unrecognized clusters. More specifically, the second, third, and sixth modules pointed to the c2 cluster as a putative mediator of cell stress and lipotoxicity.

We next explored whether cellular responses to c2 FFAs were conserved and shared between mouse MIN6 cells and human β cells *in vitro*, as well as mouse β cells *in vivo*. We found a distinct overlap of genes upregulated by c2 FFAs in MIN6 cells with (1) genes upregulated in the transcriptome of pancreatic β cells isolated from mice fed a high-fat diet[43] and (2) genes upregulated in human islets exposed to PA[28] (Figures S2E and S2F; STAR Methods).

Functional validation of FFA clustering

To functionally validate the transcriptome-derived clusters, we first measured cell viability in MIN6 cells exposed to each of the 61 FFAs (Figure 2B). The c2 FFAs induced the most consistent and significant reduction in cell numbers among all clusters. Based on the observation that FFA-induced ER stress is associated with decreased ER Ca^{2+} levels and apoptosis,[44–46] we measured ER Ca^{2+} after exposure to each of the 61 FFAs (Figure S3A; STAR Methods). We detected decreased ER Ca^{2+} levels in cells treated with c2 FFAs and, to a smaller extent, c1 FFAs, thus functionally validating the ER stress signature derived from transcriptomics (Figure 2C). In contrast, we detected a consistent increase in ER Ca^{2+} levels for cells exposed to c5 FFAs, while c3 and c4 FFAs did not alter ER Ca^{2+} levels (Figure 2C). The specific subset of 12 MUFAs in the c2 cluster caused ER Ca^{2+} deficits and cell death in contrast to c3 and c4 MUFAs (Figure 2D).

FALCON is applicable at scale to different cell types

Exposure to excess circulating FFAs has been implicated in diseases affecting many cells and organs in addition to pancreatic β cells, including the kidney[47,48] and the brain.[49–51] To assess the general versatility of FALCON, we tested two additional disease-relevant cell types: human kidney tubular epithelial cells, associated with kidney disease,[47,48] and human iPSC-derived microglia, associated with neurodegenerative disease.[49,52] In both cell types, c2 cluster FFAs were the most toxic, consistent with the results in β cells (Figures 3A–3E). Key differences included c3 and c4 FFAs universally increasing human kidney epithelial cell number (Figures 3A and 3D). In microglia, c5 PUFAs were more toxic than in β cells and kidney epithelial cells, on par with c2 FFAs (Figure 3A). Our data suggest that these critical neuro-immune cells may be particularly susceptible to PUFA-mediated injury (Figure 3A), an intriguing finding with implications for neurodegenerative diseases.[53] In sum, these studies demonstrated the utility of FALCON for multiple cell types of interest and its potential to yield fundamental insights into FFA biology.

Cell biological hallmarks of lipotoxicity characterize the newly defined c2 FFA cluster

To better understand the mechanisms underlying c2 FFA-induced toxicity universally observed in β cells, kidney epithelial cells, and microglia, we focused on erucic acid (EA), a 22-carbon

(D) Summary of functional assays. Top bar represents FFA clusters derived from transcriptomic analysis. Second color bar represents clusters derived from Cell Painting (cellular morphology) analysis (STAR Methods). Bar in grayscale indicates classical grouping of FFAs based on saturation level. The next two bars are heatmaps displaying $\log_2$ fold changes of ER Ca^{2+} levels and cell viability, respectively. x axis labels show FFA structure (in simplified molecular input line entry system [SMILES]). The box highlights the 20 FFAs in cluster 2 (c2) identified as the lipotoxicity cluster. Highlighted FFAs were chosen as cluster representatives for further downstream studies.

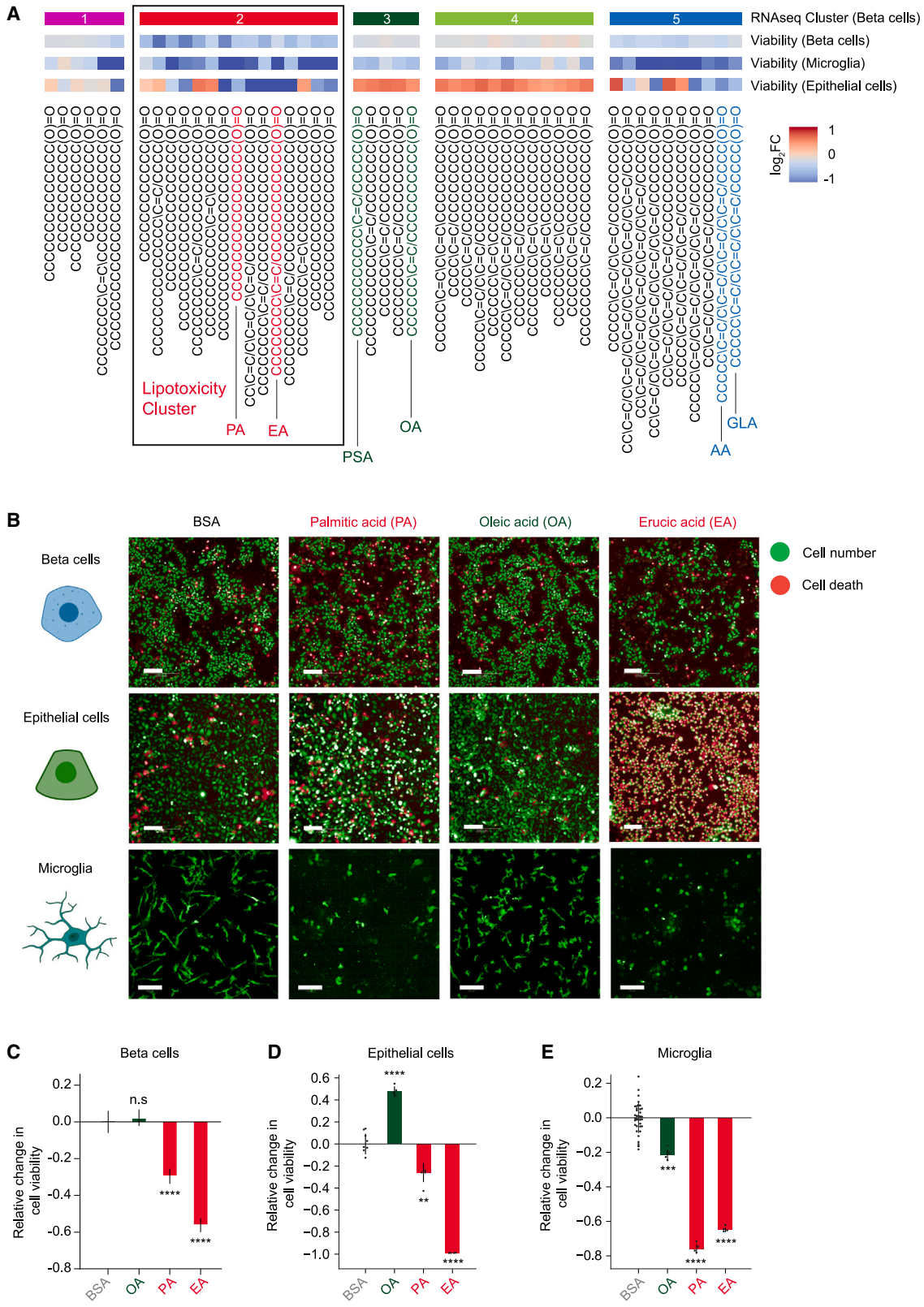

Figure 3. FALCON is applicable at scale to different cell types

(A) Heatmap showing comparison of viability changes across 3 different cell types: MIN6 pancreatic β cells, human iPSC-derived microglia, and human kidney tubular epithelial cells. c2 FFAs are toxic for all three cell types studied.

(legend continued on next page)

c2 MUFA. Although there is evidence that long-chain MUFAs such as EA are toxic,[54] the mechanisms behind this toxicity are only beginning to be explored,[26] and *in vivo* studies provide disparate pictures.[9,55] In our studies, despite its classification as an MUFA with a similar length to various c5 PUFAs, EA distinctly clustered with lipotoxic c2 FFAs. To more deeply characterize EA, we examined it in comparison with (1) PA, a saturated c2 FFA; (2) OA and petroselinic acid (PSA), two MUFAs in the non-toxic c3 cluster; and (3) arachidonic acid (AA) and gamma-linoleic acid (GLA), two long-chain FFAs in the c5 PUFA cluster. Given the high disease burden from T2D and the availability of well-characterized cellular assays (as described, for example, in Figures 1 and 2), we focused our analysis on β cells. Out of the six FFAs studied, only EA and PA consistently induced cell death (Figure 4A).

Examining the dose-dependent toxicity of EA, an FFA whose abundance in human plasma may be 10–200 times lower than PA (one of the most well-studied and abundant FFAs),[8–10] we found that as low as ~75–100-μM EA, a concentration previously measured in human plasma,[9,10] induced high levels of cell death (Figure 4B). These dose-response experiments confirmed that the biological effects we measured were physiologically relevant for PA and toxic MUFAs such as EA.

Sustained activation of the UPR has been linked to the toxicity induced by prolonged exposure to SFAs. We assessed ER stress upon exposure to FFAs by probing the cell-death-inducing PERK/ATF4/CHOP arm of the UPR.[56,57] Only treatment with EA or PA increased ATF4 and CHOP protein abundance, pointing to lipotoxicity-induced activation of the UPR (Figure 4C). In line with previous work demonstrating that depletion of ER calcium is associated with lipotoxicity-induced ER stress,[44,56] we observed significant reduction in ER Ca^{2+} levels only in cells treated with PA or EA (Figure 4D).

Lipotoxic inflammation and recruitment of immune cells into pancreatic islets plays a central role in β cell dysfunction and death in the context of T2D.[58] Based on the transcriptomic analysis (Figure 2A) and previous work with PA,[37] we focused on inflammatory signaling through NF-κB measured by nuclear translocation of RELA (p65), a major component of NF-κB-mediated transcription.[59] Robust RELA nuclear translocation was noted after treatment with EA (Figures 4E and S3B) and PA (Figure 4E). In line with the transcriptomic analysis (Figure 2A), PSA and OA triggered only modest RELA translocation (Figure 4E) without affecting cell viability (Figure 4A).

Next, we measured glucose-stimulated insulin secretion (GSIS), a function specific to β cells. Exposure to EA caused significant GSIS impairment (Figure 4F) similar to PA (Figure 4F).[60] In contrast, OA, PSA, AA, and GLA had no effect on GSIS (Figure 4F). Since impaired GSIS has been linked to disrupted autophagy,[61] and lipotoxicity increases autophagosome number,[24] we quantified LC3B-positive autophagosomes in cells exposed to FFAs. Similar to PA, EA increased autophagosome numbers, whereas OA, PSA, AA, and GLA had no effect (Figures 4G and 4H). In sum, despite structural similarities with other MUFAs or very-long-chain FFAs, EA functionally behaved like the lipotoxic saturated FFAs (as summarized in Figure 2D). Overall, these results reinforced the FFA clustering derived from systematic analyses and assigned lipotoxic effects to EA and, more broadly, to a previously unrecognized subset of 12 c2 MUFAs (Figure 2D).

c2 MUFAs are toxic to human cells

We took two additional approaches to assess the effects of toxic MUFAs such as EA in human pancreatic β cells. First, we generated human iPSC-derived β cells[62,63] and treated them with either EA (putative toxic MUFA) or OA (putative benign MUFA). Exposure to EA-induced cell death in a dose- and time-dependent manner, whereas OA had no effect on cell viability (Figures 4I and 4J). In a complementary approach, we studied human pancreatic islets acutely isolated from cadaveric donors. We treated these islets with MUFAs representing all three MUFA-containing clusters, c2, c3, and c4 (Figures 4K and 4L). Similar to MIN6 cells and iPSC-derived human β cells, c2 MUFAs (7 FFAs including EA) were toxic to human islet β cells in a dose-dependent manner, whereas c3 (OA and petroselenic acid) and c4 MUFAs (10(Z)-nonadecenoic acid) had no effect on cell viability (Figures 4K and 4L). We concluded that the c2 MUFAs can induce significant injury, making them highly relevant to human β cell biology.

Structural characterization of c2 MUFAs

We next asked whether molecular or chemical features could predict and explain this newly defined FFA grouping beyond double bond number alone. A random forest classifier trained on a matrix of 2D FFA structural features (STAR Methods) successfully predicted assignment to transcriptome-based predefined clusters c1, c2, and c5 with high sensitivity and specificity (Figures S3C; STAR Methods). This classifier showed that while the number of double bonds was an important distinguishing feature (Figures 5A, b_double), the longest chain of single bonds (b_max1len) and bond rotation (b_rotR) were highly predictive for c2 cluster assignment even among the MUFAs (c1–c4; Figure 5A). The longest chain of single bonds also reliably captured the single PUFA (13(Z), 16(Z), 19(Z)-docosatrienoic acid) that was transcriptomically assigned to c2 and predicted its separation from the rest of the PUFAs in the c5 cluster (Figure 5A).

EA induces a lipidome distinct from PA that is associated with changes in membrane fluidity

Exposure to PA leads to an increase in the abundance of saturated acyl chains of more complex lipid species.[4] This in turn is linked to the activation of the UPR, which can sense changes in lipid composition or lipid bilayer stress.[64–68] Since c2 MUFAs caused significant cellular injury, similar to PA, we hypothesized that exposure to c2 MUFAs with long single-bond chains (such as EA) may induce specific changes to the cellular lipidome that could explain their lipotoxic effect. We performed a

(B) Representative images from all 3 cell types highlighting the toxicity of c2 FFAs including erucic acid (EA). EA induces cell death in β cells (green, Hoescht), in microglia (green, GFP), and in kidney tubular epithelial cells (red, propidium iodide). Scale bars, 100 μm.
(C–E) Bar plots indicate change in cell viability relative to BSA induced by OA, PA, or EA in each cell type after exposure to FFAs at 500 μM for 72 h (MIN6) (C), 500 μM for 15 h (epithelial cells) (D), or 250 μM for 24 h (microglia) (E). PA and EA consistently induce cell death across all three cell types as assessed by one-way ANOVA followed by Dunnett's test (*$p < 0.05$, ****$p < 0.0001$). Data are mean ± SD.

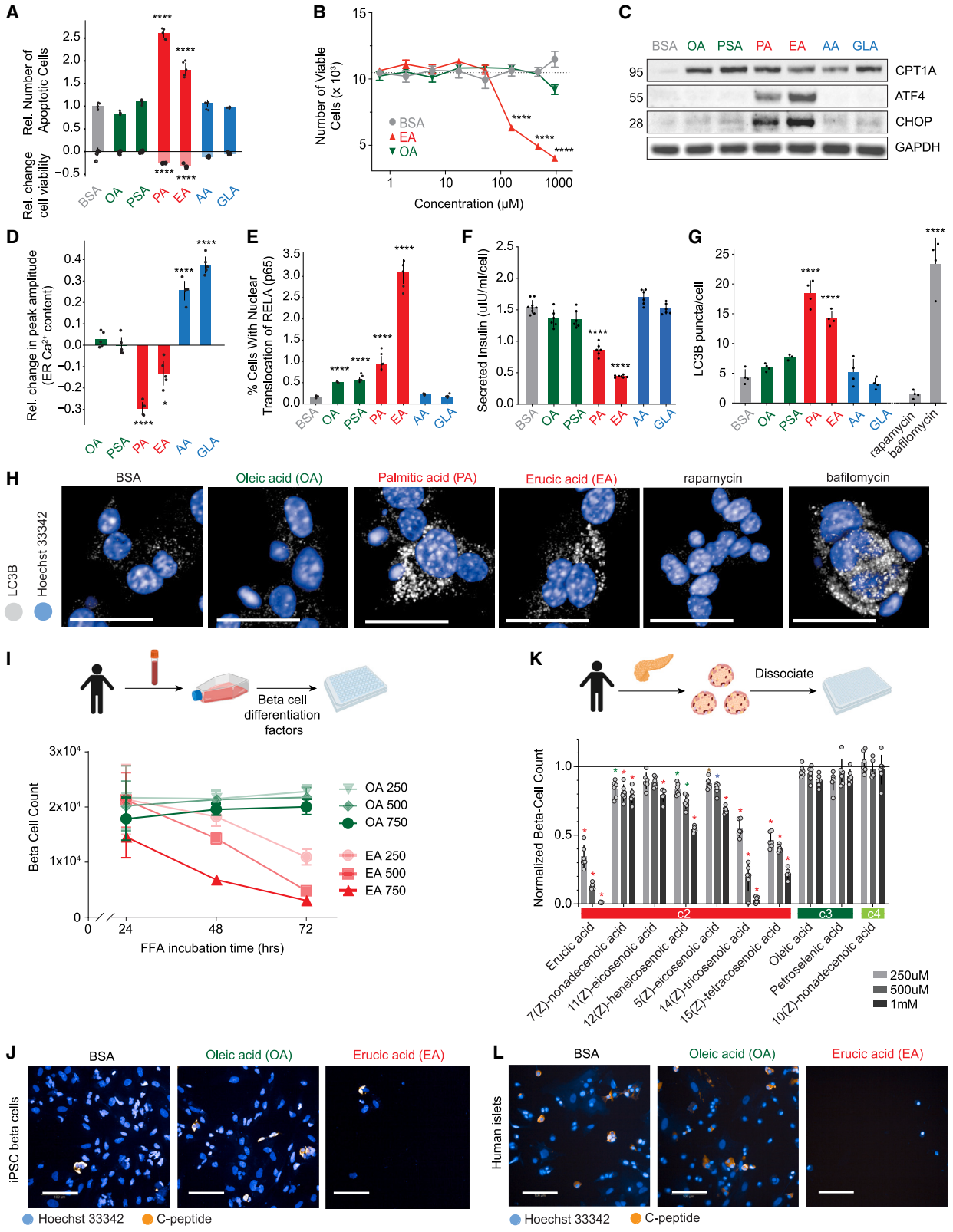

Figure 4. Cell biological hallmarks of lipotoxicity characterize the c2 FFA cluster

(A) Cell viability after treatment with representative FFAs for 48 h. Percentage of apoptotic cells (positive y axis) and reduction in cell viability (negative y axis) are presented. Data are mean ± SD. Student's t test (two-sided), ****p < 0.0001, corrected for multiple testing (Bonferroni), n = 5 wells.

(legend continued on next page)

lipidomics analysis and found that exposure of cells to EA led to the accumulation of longer, unsaturated acyl chains in multiple lipid classes (DAGs, PCs, and PEs), and especially in TAGs (Figures 5B and S3D). This profile was consistent with the integration of the very-long-chain unsaturated EA into more complex lipids and represented a lipidome distinct from that induced by PA (Figure 5B; Table S2).

To probe the functional consequences of incorporation of long-chain FFAs into the lipidome, we measured membrane fluidity using a Laurdan dye that fluoresces at different wavelengths in accordance with lipid order/disorder, following a protocol previously used to demonstrate maladaptive PA-induced membrane rigidity.[69,70] Notably, EA had a unique biphasic effect on membrane fluidity. At the lowest concentrations, EA was similar to OA with a trend toward increasing membrane fluidity (Figure 5C). At higher concentrations, similar to those measured in plasma from patients on FFA-rich diet[9,10] (and at which we found that EA is toxic; Figure 4B), membrane fluidity was decreased (Figure 5C). Exposure to PA led to linear regions of increased rigidity reminiscent of the ER[71,72] (Figure S3E), while EA induced distinct spherical regions of increased rigidity reminiscent of lipid droplet morphology (Figure S3E). These observations are consistent with robust EA incorporation into TAGs (Figure 5B). In sum, we found that exposure to EA generated a distinct cellular lipidome characterized by species with long unsaturated acyl chains that induced toxicity by decreasing cellular membrane fluidity.

Identification of genes at the intersection of FFA exposure and genetic risk for metabolic disease

Complex diseases arise from the interaction of genetic risk and environmental exposures.[73] GWAS have greatly contributed to our understanding of the genomic architecture of complex diseases,[74] including T2D.[12,75,76] While several T2D genomic studies have shown a strong association with loci linked to β cell function,[13,77–79] it remains challenging to annotate variants and prioritize genes for mechanistic functional follow-up studies (https://www.icda.bio/).

In our experiments, β cell exposure to 20 c2 FFAs significantly up- or downregulated specific genes (Figures 2A and S2A). We hypothesized that a subset of these genes could also be implicated in genetic risk for T2D. We therefore sought to prioritize disease-relevant genes by investigating the overlap between an annotated large-scale T2D GWAS dataset[80] and genes highlighted by our transcriptomic analysis (Figures 2A and S2A).

We ranked putative T2D genes using MAGMA software (STAR Methods)[22] and used the gene set analysis (GSA) function[22] to test whether the β cell c2 FFA transcriptomic signature was enriched in the MAGMA-ranked T2D genes. Overlapping the two datasets revealed that the top 5% of significantly differentially expressed lipotoxicity genes were enriched among the T2D GWAS ranked genes (FDR < 0.001; Figure 6A). This enrichment was specific to T2D as opposed to GWAS datasets for autoimmune type 1 diabetes[81] or schizophrenia, an unrelated neurodevelopmental disorder[82] (Figure 6A). T2D GWAS genes were specifically enriched in the c2 cluster signature but not in that of the other four clusters (Figure 6B). Plotting the genes that drove this enrichment according to their MAGMA rank on the x axis (Table S3) and their lipotoxicity rank on the y axis (based on differential expression p value; Figure 6C; Table S4), we identified 25 genes at the intersection of lipotoxicity and T2D (Figures 6C and 6D).

Our sensitivity for gene detection was greatly enhanced by the integrated transcriptome derived from all 20 c2 FFAs used to construct the lipotoxicity signature. Accordingly, the transcriptomic signature generated by PA treatment alone predicted only 6 of the 25 T2D-lipotoxicity genes, thus missing 19 important gene candidates including *GLP1R*, *SLC30A8*, *ADCY5*, and *CMIP* (Figure 6E). Our analysis indicates that these genes which are of high interest for T2D, may also be relevant in the context of lipotoxicity. Of the T2D-lipotoxicity genes revealed by our analysis, we focused our next set of experiments on *CMIP* because

(B) Dose-response curve of viable cell numbers after 65 h of EA or OA treatment compared with BSA. EA is toxic in a concentration-dependent manner; OA is not toxic.
(C) Western blots show ATF4 and CHOP induction by PA and EA (lipotoxic c2 FFAs). CPT1A induction is a control for intracellular FFA delivery. BSA, negative control.
(D) Quantification of peak amplitude as readout for ER Ca^{2+} levels, relative to negative control (BSA). Data are mean ± SD. Student's t test (two-sided), *p < 0.05, ****p < 0.0001, corrected for multiple testing (Benjamini-Hochberg, entire FFA library).
(E) Quantification of RELA translocation as percentage of total number of cells (t = 18 h, n = 5 replicates). Data are mean ± SD. Student's t test (two-sided), ****p < 0.0001, corrected for multiple testing (Bonferroni).
(F) Glucose-stimulated insulin secretion (GSIS) after FFA exposure (FFA = 500 μM, t = 24 h, n = 6 wells) was measured by ELISA.
(G) Autophagosome formation was assessed by imaging LC3B puncta normalized to the number of total cells (t = 48 h, n = 4 wells). Data are mean ± SD. One-way ANOVA followed by Dunnett's test.
For (A) and (D)–(G), bar color represents cluster identity (green, c3; red, c2; blue, c5; Figure 1D).
(H) Representative images of LC3B immunofluorescence (gray) in MIN6 cells treated with FFAs, BSA as negative control, or autophagy-modulating drugs. Nuclei were detected by Hoechst (blue). c2 FFAs induce autophagosomes. Scale bars, 25 μm.
(I) Number of iPSC-derived β cells after exposure to EA or OA for 24, 48, or 72 h at 250, 500, or 750 μM. Only EA decreased cell count in a dose- and time-dependent manner. All EA conditions are significant per two-way ANOVA (p < 0.0001); all OA conditions are not significant. Data are mean ± SD, n = 4–6 wells/time point/FFA.
(J) Representative images of iPSC-derived β cells after treatment with BSA, EA, or OA for 48 h at 500 μM. Nuclei are marked by Hoechst and β cell identity is marked by C-peptide staining (orange). Scale bars, 100 μm.
(K) Quantification of C-peptide positive cells human β cells dissociated from cadaveric primary islets normalized to the BSA control after exposure to each of 10 FFAs at 3 different concentrations (t = 5 days, n = 6 wells). c2 cluster MUFAs decreased human β cell viability in a dose-dependent manner. Data are mean ± SD. Multiple t test with Bonferroni correction (gold, p < 0.05; blue, p < 0.01; green, p < 0.001; red, p < 0.0001).
(L) Representative images of human islets after treatment with BSA, EA, or OA. Nuclei are marked by Hoechst, and β cell identity is marked by C-peptide staining (orange). Scale bars, 100 μm.

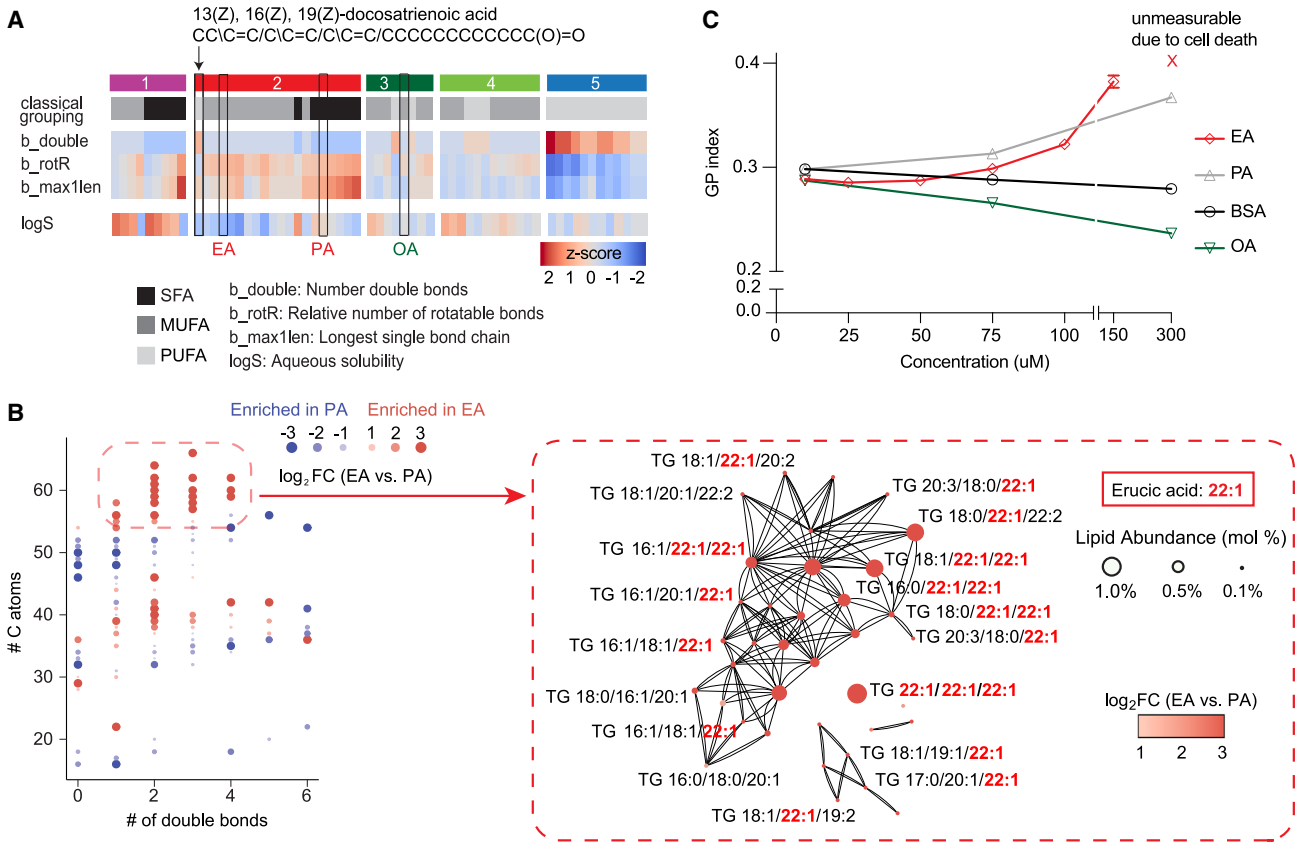

Figure 5. Long single-bond chain in MUFA (EA) induces a distinct lipidomic profile that is associated with increased membrane rigidity

(A) Selected features from the decision tree analysis based on meta-features of highest importance (mean decrease accuracy; STAR Methods). The longest single-bond chain is the meta-feature that predicts the inclusion of 13(Z), 16(Z), 19(Z)-docosatrienoic acid as the only PUFA in the c2 cluster and distinguishes between toxic EA and non-toxic OA.

(B) Accumulation of longer unsaturated acyl chains found by lipidomic analysis of MIN6 cells treated for 24 h with 500 μM EA (left). A network analysis of the biochemical relationship (lines) between significantly enriched lipid species in the EA-induced lipidome highlighted the accumulation of EA (22:1)-containing triglyceride (TG) species (right).

(C) Membrane rigidity as measured by the GP index of Laurdan dye in INS1E β cells after 12 h treatment with 3–6 different concentrations of BSA, PA, EA, or OA. PA increases membrane rigidity proportionally to its concentration; EA decreases membrane rigidity at low concentration similar to OA; but at higher, toxic levels EA increases membrane rigidity similar to PA. Data are mean ± SEM; n = 6 wells.

(1) it had not been previously implicated in β cell biology (despite its possible association with the islet MAF transcription factor family[83]) and (2) it had no known role in lipotoxicity, thus offering opportunities for new biological insights.

CMIP suppresses lipotoxicity in β cells

CMIP has been implicated in kidney disease[84,85] and cancer,[86] but it has not been studied in β cells. Of interest, *CMIP*-associated risk loci are linked to alterations in body mass index[87] and dyslipidemia.[88] In immune cells, CMIP interacts with RELA and reduces NF-κB activation.[89] A genome-wide interaction analysis with the insulin secretion locus *MTNR1B* identified an interaction with a *CMIP* intronic SNP affecting T2D risk.[90] To study CMIP in β cells, we generated MIN6 *Cmip* knockout cell lines and isolated one *Cmip* knockout (CMIP KO) clone with a complete deletion of the major CMIP isoform (Figure S4A). At baseline, this CMIP KO line and the non-targeting guide WT control (1) displayed similar morphology (Figure S4B), (2) expressed key β cell markers (qPCR; Figure S4C), (3) responded to high glucose by a 2-fold increase in GSIS (Figure S4D), and (4) showed similar doubling rates in culture (Figure 7A). Thus, at baseline CMIP is not required for β cell survival or insulin secretion. In contrast, *Cmip* deletion significantly increased sensitivity to lipotoxic stress and cell death (Figures 7B and 7C). Specifically, *Cmip* deletion exacerbated the lipotoxic effects of PA and EA and converted the typically non-toxic c3 MUFAs OA and PSA into toxic FFAs (Figure 7B). Functionally, *Cmip* deletion increased NF-κB signaling (Figures 7D and S4F).[89] Exposure to PA or EA, but not PSA or OA, increased RELA nuclear translocation in CMIP KO cells more than 4-fold compared with WT controls (Figure S4F). Thus, *Cmip* deletion increased inflammatory signaling in β cells in response to lipotoxic FFAs. *Cmip* deletion also worsened the EA- or PA-induced reduction in insulin secretion (Figure 7E).

Restoring CMIP abundance in CMIP KO cells (as quantified in Figure S4G) led to a partial rescue from EA-induced cell death (Figure 7F) and a faster decline in EA-induced inflammatory NF-κB signaling (Figure S4I; no effect on NF-κB signaling in the absence of EA; Figure S4H). Similarly, GSIS was improved

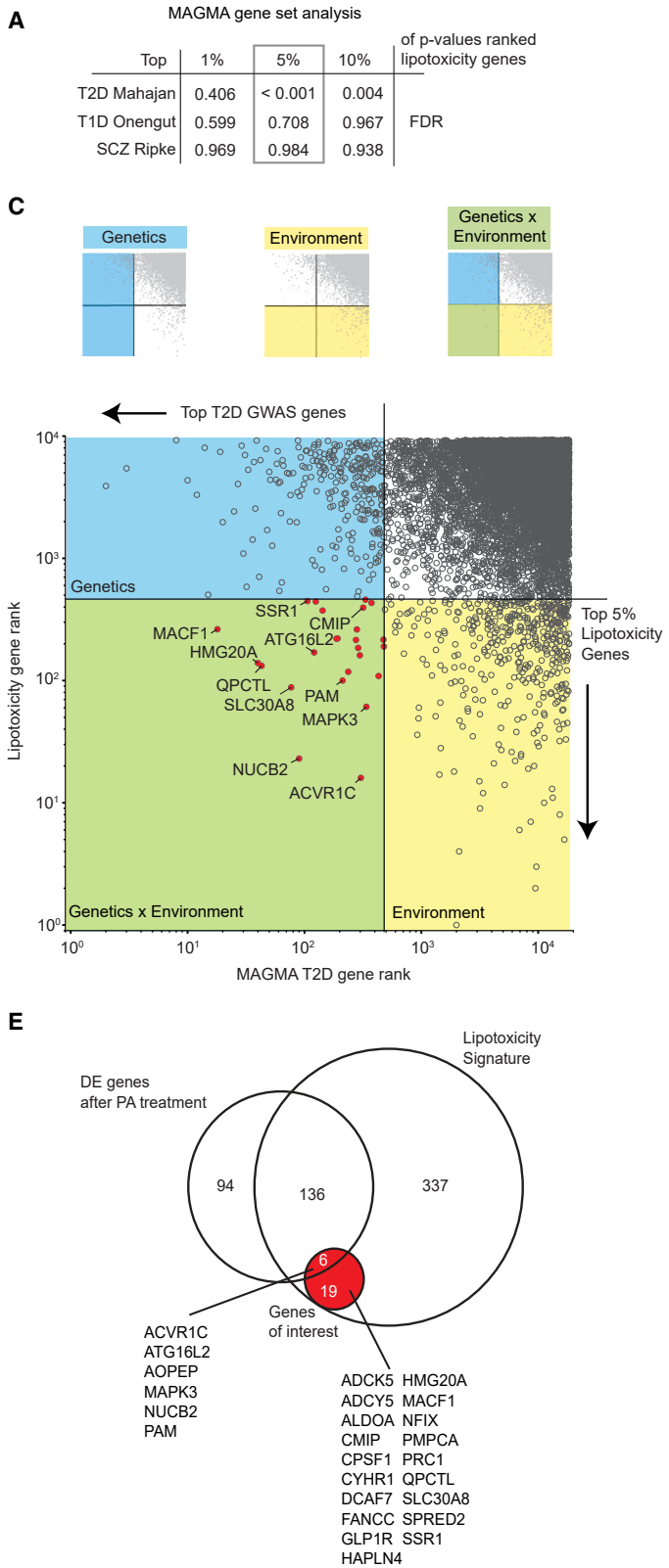

(legend on next page)

upon restoring CMIP expression, especially in EA-treated cells (Figure 7G). Taken together, these data revealed that *CMIP*, initially found among thousands of loci in a T2D GWAS, could now be prioritized as a putative suppressor of lipotoxic injury in β cells.

To gain insights into CMIP's function in β cells, we analyzed *CMIP* gene expression from human islets,[91] which correlated with several pathways including PI3K-Akt signaling, insulin secretion, FFA metabolism, and AMPK signaling (Figures S4J and S4K). Intriguingly, consistent with prior work in peripheral blood mononuclear cells,[92] we found that the regulatory subunit of PI3K (p85α) co-immunoprecipitated with CMIP in β cells (Figure 7H), suggesting that this interaction may connect CMIP to metabolic signaling pathways (Figures S4J and S4K).

To experimentally probe these pathways, we assessed the activity of three critical metabolic sensors in β cells: AMPKα, Akt, and FOXO1. AMPKα and FOXO1 signaling were unchanged after CMIP deletion (Figure S4L). In contrast, *Cmip* deletion resulted in increased phosphorylated Akt (pAkt) protein abundance (with no effect on total Akt; Figure 7I). Interestingly, pAkt in WT cells exposed to EA was at the same level as pAkt in CMIP KO cells at baseline (Figure 7I). When exposed to EA, CMIP KO cells could not increase pAkt further (Figure 7I). Since modulation of Akt signaling in response to metabolic stress is thought to promote β cell survival[93,94] and PI3K activity increases the presence of phosphoinositide signaling molecules (PIP_2 and PIP_3) in the plasma membrane to recruit Akt for activation and downstream signaling,[95] the simplest explanation for our data is that CMIP modulates Akt activity through its interaction with PI3K. Upon *Cmip* deletion, cells lose the ability to dynamically regulate Akt, making them more vulnerable to FFA-induced cell death compared with WT β cells (Figure 7B).

As a final test, and to probe for the human relevance of CMIP, we generated human iPSC-derived β cells in which *CMIP* was deleted. In these human cells, *CMIP* deletion reduced cell viability after treatment with either EA or OA (Figures 7J and 7K).

DISCUSSION

Lipids, including FFAs, are ubiquitous in living organisms and essential for life, yet significant knowledge gaps remain in our understanding of FFA biology. In this study, we pioneered FALCON, a multimodal, systematic approach to functionally characterize structurally diverse FFAs. Our approach was comprehensive both in input (number of FFAs tested) and output (multimodal readouts). The added dimensionality—a direct consequence of studying the effects of 61 diverse FFAs—provided the necessary power to uncover biological features across the entire spectrum of FFAs tested. Our studies led to several important conclusions.

First, 20 structurally diverse FFAs defined the toxic (c2) cluster, a group of FFAs united solely by the fact that they mediated similar functional outcomes. The identification of MUFAs in the c2 cluster (12/20 FFAs) suggests a shift in how we interpret the toxicity of FFAs because we show that saturation alone is not sufficient to predict the lipotoxic potential of a given FFA. MUFAs like OA have been proposed to have harmless or even beneficial effects.[3] However, our experiments, including studies in human islets, kidney epithelial cells, and microglia showed that OA is not representative of the entire MUFA class and highlighted several MUFAs, such as EA, that were highly toxic. Our classifier (Figure S3C) suggests that double-bond-containing MUFAs with a long stretch of carbons linked by single bonds are functionally similar to SFAs, at least in terms of cellular toxicity. In contrast to the well-known accumulation of saturated acyl chains after PA treatment,[4] the EA lipidome was characterized by an accumulation of long-chain unsaturated acyl chains. The membrane fluidity studies revealed that at low concentrations, EA behaves like non-toxic MUFAs (e.g., OA), but at higher concentrations, EA becomes harmful because the incorporation of its long unsaturated chains into complex lipid species changes the properties of lipid membranes in a manner similar to SFAs (e.g., PA). The resulting increase in membrane rigidity likely contributes to lipid bilayer stress culminating in activation of cell death pathways.[66] Future work may test whether increased membrane rigidity at high concentrations of EA is directly related to the predicted impact of incorporating its long chain of single bonds (Figure S3C) into membrane lipids.

Second, the comprehensive interrogation of many FFAs with FALCON allowed us to gain new biological insights. Due to the large number of FFAs studied simultaneously (e.g., 20 c2 toxic FFAs), we gained power well beyond that achievable by interrogating the effects of a single FFA alone (such as PA; Figure 6E). Accordingly, we identified a set of 25 genes that are transcriptionally responsive to lipotoxic stress and are also associated with variants that confer genetic risk for T2D. Our analysis identified a link between lipotoxicity and several T2D genes such as *GLP1R*, a well-known obesity[96] and T2D drug target,[97] and *SLC30A8*, a gene in which coding variants have been shown to

Figure 6. Integration of lipotoxicity transcriptomic signature with T2D GWAS dataset identifies *CMIP* as mediator of genetic and environmental risk for disease

(A) Gene set analysis (GSA) results based on the c2 lipotoxicity signature. T2D GWAS genes were ranked based on MAGMA score. A T1D and a schizophrenia GWAS dataset served as negative controls. Lipotoxicity gene sets are defined as top DE genes (1%, 5%, and 10%) in transcriptomic profiles from the c2 cluster ranked by p value and $\log_2$ fold change (LFC). GSA showed significant enrichment (FDR < 0.05) for the top 5% (boxed) and 10% lipotoxicity gene sets.

(B) Enrichment analysis for all FFA clusters (top 5% gene set) revealed that the c2 cluster gene set is uniquely enriched in the T2D GWAS dataset.

(C) Scatterplot of genes based on T2D MAGMA rank (x axis) and lipotoxicity rank (y axis). Horizontal boundary defines top 5% lipotoxicity signature genes, vertical boundary defines top 600 MAGMA-ranked T2D genes. As demonstrated in the schematic (top), genes located in the left (blue) quadrants are associated with T2D genetic risk, genes located in the bottom (yellow) quadrants are associated with lipotoxicity environmental risk, and genes located in the bottom left (green) quadrant are associated with both genetic and environmental risk. Genes of interest (red) drove the enrichment of the lipotoxicity signature in the GWAS dataset.

(D) Expression pattern for the top 25 overlapping T2D-lipotoxicity genes across all FFA clusters. Size of dots represents the percentage of FFAs/cluster that induce significant differential expression of corresponding gene ($p < 0.05$, Benjamini-Hochberg); colors represent strength and directionality of transcriptional changes ($\log_2$ fold change).

(E) Venn diagram comparing the results of the analysis using the PA-induced signature alone compared with using the c2 lipotoxicity signature derived from all 20 lipotoxic FFAs. 19/25 genes, including *GLP1R* and *CMIP*, would have been missed if the analysis was limited to the PA-induced signature alone.

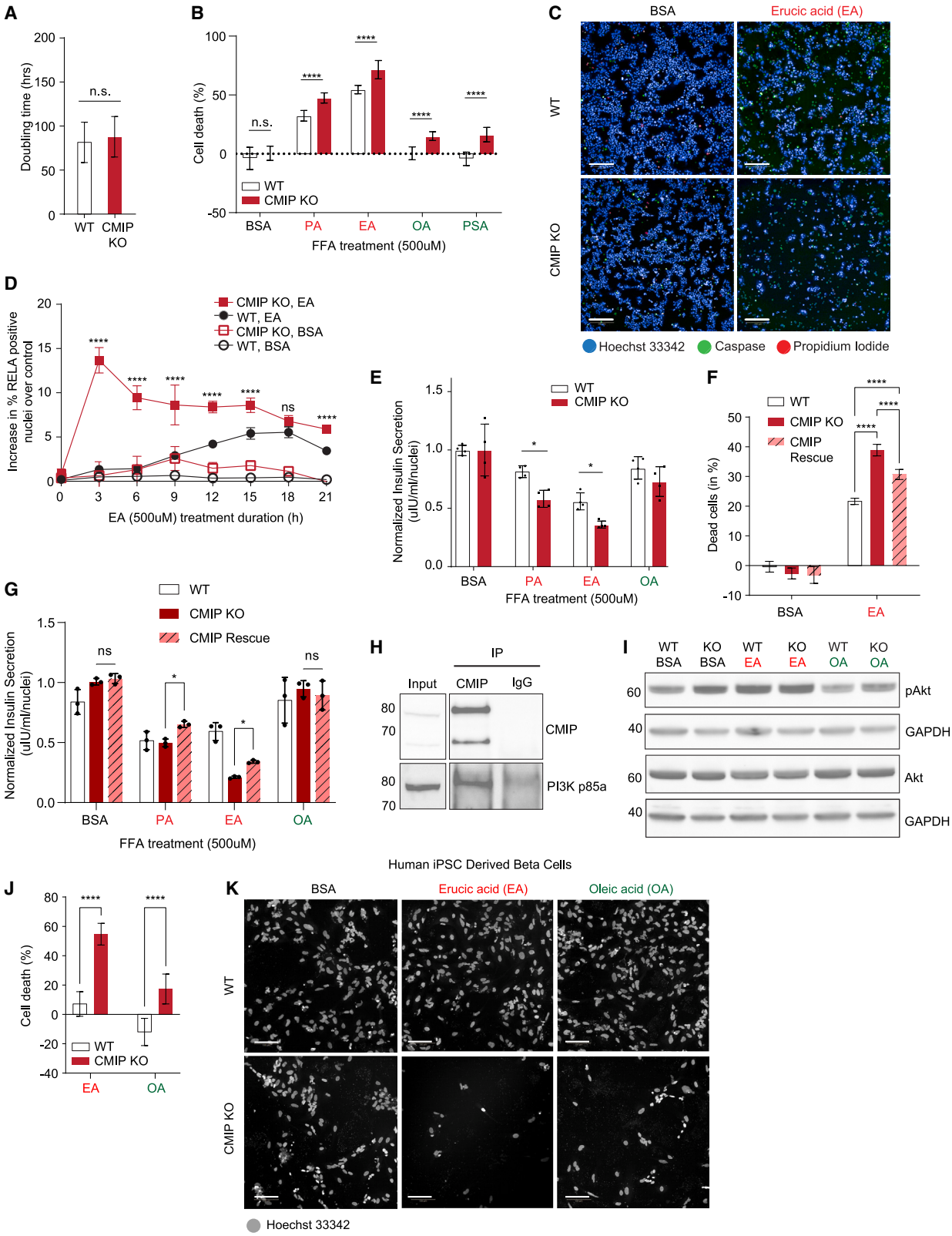

(legend on next page)

modify risk for T2D.[77,78,98] Importantly, we identified CMIP as a previously unrecognized suppressor of lipotoxicity, and we confirmed that these findings are relevant to humans using iPSC-derived β cells. Future studies will focus on the precise molecular mechanism by which CMIP senses FFAs and modulates Akt and related pathways. This proof-of-concept study illustrates FALCON's ability to prioritize genes of high mechanistic value that may have otherwise gone unnoticed based on genomics data alone and offers a method for prioritizing targets that reflect the combined effects of environmental exposure and genetic risk for disease.

Third, FALCON can serve as a valuable tool for exploring fundamental lipid biology in different cell types and tissues. Lipotoxicity and alterations in lipid metabolism have been implicated in numerous disorders including kidney disease,[99,100] neuropathy,[101] cancer,[27,102,103] liver disease,[104] and Alzheimer's disease.[105–110] However, many of the fundamental mechanisms involving lipotoxic FFAs in these diseases have yet to be fully elucidated.[111] For example, metabolic alterations in cancer cells that increase fatty acid synthesis and uptake have long been correlated with cancer progression.[102,112] In other tissues, such as the heart, studies exploring the mechanisms underlying lipotoxic cardiomyopathy have explicitly called for investigations into the contributions of individual fatty acids to disease pathogenesis.[113] FALCON provides the fatty acid level resolution necessary to begin to tackle these complex questions across many cell types and diseases of interest.

Finally, an important translational implication of our study is the notion that the precise FFA profiles in human blood or tissue may carry valuable information about personalized disease risk and progression. The application of FALCON to the interpretation of patient-derived FFA profiles in the future may facilitate the implementation of personalized medicine in metabolic disease.

Limitations of study

Since some FFAs in our platform are protective while others are harmful, the study of FFA combinations may be of interest. We note that the large number of potential FFA combinations (>1,800) currently limits the feasibility of such a systematic study, but future work may prioritize some FFA combinations for follow-up work.

While the work described here was largely focused on c2 FFAs, we uncovered many additional biological processes that merit further study, for example, the putative role of ferroptosis induced by c5 PUFAs in microglia. By making all of our datasets publicly available, we hope that many colleagues in the scientific community will be empowered to explore them further.

Finally, although we validated our work with CMIP in human pancreatic β cells, further experiments will determine the human relevance of CMIP. The importance of the other T2D-lipotoxicity genes in the pathogenesis of metabolic disease will be explored in future studies.

STAR★METHODS

Detailed methods are provided in the online version of this paper and include the following:

- KEY RESOURCES TABLE
- RESOURCE AVAILABILITY
  - Lead Contact
  - Materials Availability
  - Data and code availability
- EXPERIMENTAL MODEL AND SUBJECT DETAILS
  - Cell lines
  - iPSC-derived cells
  - Primary cells
- METHOD DETAILS
  - FFA Preparation
  - Differential Scanning Calorimetry
  - Lipid Profiling
  - RNASeq
  - Cell Painting
  - CMIP KO Clone Selection

Figure 7. *Cmip* deletion sensitizes β cells to FFA-mediated injury and cell death

(A) *Cmip* deletion does not affect cell proliferation. Two-sided t test, n = 19 passages.

(B) After exposure to lipotoxic PA or EA, cell death is increased in CMIP KO compared with WT cells. Non-toxic OA and PSA are rendered toxic in CMIP KO cells. Cell death was measured as percentage of viable cells compared with the non-treated control for WT and CMIP KO cells after 72 h exposure to FFAs (500 μM, n = 21 wells). Data are mean ± SD. Two-way ANOVA with multiple comparisons (Šídák correction,****$p < 0.0001$).

(C) Representative images of the cell death assay showing increased susceptibility to EA in CMIP KO cells. Stains include nuclei (Hoechst, blue), apoptotic cells (caspase 3/7, green), and dead cells (propidium iodide, red). Scale bars, 100 μm.

(D) Percentage of cells with RELA nuclear translocation after exposure to EA or BSA (500 μM) at 3 h intervals. Data are mean ± SD, n = 7 wells. Two-way ANOVA with multiple comparisons (Šídák correction, ****$p < 0.0001$).

(E) Normalized insulin secretion at baseline after 24 h treatment with FFA (500 μM). Insulin secretion was reduced in CMIP KO cells upon exposure to lipotoxic FFAs. Data are mean ± SD. Two-way ANOVA with multiple comparisons (Holm-Šídák correction, *$p < 0.05$).

(F) Reintroduction of CMIP in CMIP KO cells (CMIP rescue) attenuates the toxic effects of EA. Percentage of cell death after 24 h exposure to FFAs (250 μM, n = 9 wells). Data are mean ± SD. Two-way ANOVA with multiple comparisons (Tukey correction, ****$p < 0.0001$).

(G) CMIP rescue partially restores insulin secretion in cells exposed to c2 FFAs. Normalized glucose-stimulated insulin secretion in WT and CMIP KO cells after 24 h treatment with FFA (500 μM). Data are mean ± SD. Two-way ANOVA with Šídák multiple comparison test (*$p < 0.05$, n = 3 wells).

(H) PI3K p85α immunoprecipitates with CMIP in β cells. Western blot displaying lysate input (left) or coimmunoprecipitation (coIP) with a CMIP or IgG control antibody (right) stained for CMIP (top) or PI3K (bottom) (n = 3 blots).

(I) Phosphorylated Akt (pAkt) abundance is increased in CMIP KO cells compared with WT controls. EA exposure increases pAkt in WT cells, but not in CMIP KO cells indicating that CMIP deletion maximizes pAkt levels at baseline. Western blot for pAkt and total Akt after 24 h treatment with 500 μM FFAs (GAPDH, loading control; n = 3 blots).

(J) In human iPSC-derived β cells, CMIP KO promotes cell death, in agreement with experiments in MIN6 β cells (B). Cell death in human iPSC-derived β cells after treatment with BSA, EA, or OA at 500 μM for 24 h (n = 24 wells). (****$p < 0.0001$, two-way ANOVA with Bonferroni multiple comparison test).

(K) Representative images of cell death assay in human iPSC-derived β cells as measured by number of nuclei (Hoechst). Scale bars, 100 μm.

- CMIP Overexpression for Rescue Studies
- Cell Viability
- Western Blot
- Coimmunoprecipitation (co-IP)
- Immunofluorescence (IF) staining
- ER Calcium Levels
- Glucose Stimulated Insulin Secretion (GSIS)
- Membrane Fluidity Assay

- QUANTIFICATION AND STATISTICAL ANALYSIS
  - Lipidomics
  - RNASeq pipeline
  - Gene Set Enrichment Analysis
  - Rank-rank hypergeometric overlap (RRHO)
  - Structural analysis of FFAs
  - Morphological feature analysis
  - MAGMA analysis pipeline

SUPPLEMENTAL INFORMATION

Supplemental information can be found online at https://doi.org/10.1016/j.cmet.2023.03.018.

ACKNOWLEDGMENTS

We thank Katie Liguori for excellent graphic design work and colleagues in the Center for the Development of Therapeutics for their assistance in the preparation of the FFA library. This work was supported by a seed grant from the Broad Institute of MIT and Harvard (B*n*10), DK095045, DK099465, and Cure Alzheimer's Fund (to A.G.). N.W. was supported by a Deutsche Forschungsgesellschaft Fellowship (WI 4612/1-1) and is a participant in the BIH Digital Clinician Scientist Program funded by the DFG, Charité – Universitätsmedizin Berlin and the Berlin Institute of Health at Charité (BIH). J.C.F. and J.C.R. were supported by the National Institute of General Medical Sciences (T32GM007753 to both and T32GM007726 to J.C.F.). E.-H.S., C.K., and M.R.B. were supported by the National Institutes of Health (F30DK112477, F31DK126252, and K00DK123834, respectively). M.D.-L. was supported by a Broad-Israeli Science Foundation Fellowship. E.S. was supported by NIH 1-R01-DK126855-01 and an American Surgical Association Foundation Fellowship. M.C. was supported by FNIH AMP-T2D RFB8b and NIDDK UM1 DK126185. A.E.C. and S.S. were supported by the National Institutes of Health (NIH MIRA R35 GM122547). R.D. was supported by the Knut and Alice Wallenberg Foundation, Sweden (KAW 2019.0580). The content is solely the responsibility of the authors and does not necessarily represent the official views of the National Institutes of Health.

AUTHOR CONTRIBUTIONS

N.W., J.C.F., J.L.P., and A.G. conceived the study and designed the experiments. N.W. and J.C.F. conducted experiments and analyzed the data; experimental work was contributed by C.K., E.-H.S., J.L.M., M.D.-L., J. Sieber, J.P., J.L.P., J.C.R., M.T., H.Y., Z.W.L., A.B., R.D., J. Small, V.S., M.H., and D.L.; data analysis was contributed by C.K., E.-H.S., M.R.B., C.A., M.K.-A., K.R.G., C.C., H.S.A., S.S., R.S., A.C., J.F., and J.L.P. N.W., J.C.F., J.L.P., J.L.S., and A.G. wrote the manuscript; A.G. directed the study. All authors read the manuscript and approved its contents.

DECLARATION OF INTERESTS

N.W., J.C.F., and A.G. are co-inventors of a patent on the composition, method, and use for FFA screening, application no: 52199-550P01US. A.G. serves as a founding advisor to a new company launched by Atlas Ventures, an agreement reviewed and managed by Brigham and Women's Hospital, Mass General Brigham, and the Broad Institute of MIT and Harvard in accordance with their conflict of interest policies.

INCLUSION AND DIVERSITY

We support inclusive, diverse, and equitable conduct of research.

Received: July 27, 2022
Revised: February 21, 2023
Accepted: March 27, 2023
Published: April 18, 2023

REFERENCES

1. Lytrivi, M., Castell, A.L., Poitout, V., and Cnop, M. (2020). Recent insights into mechanisms of β-cell lipo- and glucolipotoxicity in type 2 diabetes. J. Mol. Biol. *432*, 1514–1534. https://doi.org/10.1016/j.jmb.2019.09.016.
2. Sharma, R.B., and Alonso, L.C. (2014). Lipotoxicity in the pancreatic beta cell: not just survival and function, but proliferation as well? Curr. Diab. Rep. *14*, 492.
3. Palomer, X., Pizarro-Delgado, J., Barroso, E., and Vázquez-Carrera, M. (2018). Palmitic and oleic acid: the yin and yang of fatty acids in type 2 diabetes mellitus. Trends Endocrinol. Metab. *29*, 178–190. https://doi.org/10.1016/j.tem.2017.11.009.
4. Piccolis, M., Bond, L.M., Kampmann, M., Pulimeno, P., Chitraju, C., Jayson, C.B.K., Vaites, L.P., Boland, S., Lai, Z.W., Gabriel, K.R., et al. (2019). Probing the global cellular responses to lipotoxicity caused by saturated fatty acids. Mol. Cell *74*, 32–44.e8.
5. Rhee, E.P., Cheng, S., Larson, M.G., Walford, G.A., Lewis, G.D., McCabe, E., Yang, E., Farrell, L., Fox, C.S., O'Donnell, C.J., et al. (2011). Lipid profiling identifies a triacylglycerol signature of insulin resistance and improves diabetes prediction in humans. J. Clin. Invest. *121*, 1402–1411.
6. Saponaro, C., Gaggini, M., Carli, F., and Gastaldelli, A. (2015). The subtle balance between lipolysis and lipogenesis: a critical point in metabolic homeostasis. Nutrients *7*, 9453–9474.
7. Al-Sulaiti, H., Diboun, I., Banu, S., Al-Emadi, M., Amani, P., Harvey, T.M., Dömling, A.S., Latiff, A., and Elrayess, M.A. (2018). Triglyceride profiling in adipose tissues from obese insulin sensitive, insulin resistant and type 2 diabetes mellitus individuals. J. Transl. Med. *16*, 175.
8. Abdelmagid, S.A., Clarke, S.E., Nielsen, D.E., Badawi, A., El-Sohemy, A., Mutch, D.M., and Ma, D.W.L. (2015). Comprehensive profiling of plasma fatty acid concentrations in young healthy Canadian adults. PLoS One *10*, e0116195. https://doi.org/10.1371/journal.pone.0116195.
9. Aubourg, P., Adamsbaum, C., Lavallard-Rousseau, M.-C., Rocchiccioli, F., Cartier, N., Jambaqué, I., Jakobezak, C., Lemaitre, A., Boureau, F., and Wolf, C. (1993). A two-year trial of oleic and erucic acids ("Lorenzo's Oil") as treatment for adrenomyeloneuropathy. N. Engl. J. Med. *329*, 745–752.
10. Lust, C.A.C., Bi, X., Henry, C.J., and Ma, D.W.L. (2021). Development of fatty acid reference ranges and relationship with lipid biomarkers in middle-aged healthy Singaporean men and women. Nutrients *13*, 435. https://doi.org/10.3390/nu13020435.
11. da Silva Rosa, S.C., Nayak, N., Caymo, A.M., and Gordon, J.W. (2020). Mechanisms of muscle insulin resistance and the cross-talk with liver and adipose tissue. Physiol. Rep. *8*, e14607.
12. Petrie, J.R., Pearson, E.R., and Sutherland, C. (2011). Implications of genome wide association studies for the understanding of type 2 diabetes pathophysiology. Biochem. Pharmacol. *81*, 471–477.
13. Pasquali, L., Gaulton, K.J., Rodríguez-Seguí, S.A., Mularoni, L., Miguel-Escalada, I., Akerman, İ., Tena, J.J., Morán, I., Gómez-Marín, C., van de Bunt, M., et al. (2014). Pancreatic islet enhancer clusters enriched in type 2 diabetes risk-associated variants. Nat. Genet. *46*, 136–143.
14. Udler, M.S., Kim, J., von Grotthuss, M., Bonàs-Guarch, S., Cole, J.B., Chiou, J., Christopher D. Anderson on behalf of METASTROKE and the ISGC, Boehnke, M., Laakso, M., Atzmon, G., et al. (2018). Type 2 diabetes genetic loci informed by multi-trait associations point to disease

mechanisms and subtypes: a soft clustering analysis. PLoS Med. *15*, e1002654.

15. Parker, S.C.J., Stitzel, M.L., Taylor, D.L., Orozco, J.M., Erdos, M.R., Akiyama, J.A., van Bueren, K.L., Chines, P.S., Narisu, N., et al.; NISC; Comparative; Sequencing Program (2013). Chromatin stretch enhancer states drive cell-specific gene regulation and harbor human disease risk variants. Proc. Natl. Acad. Sci. USA *110*, 17921–17926.
16. Prentki, M., and Madiraju, S.R.M. (2012). Glycerolipid/free fatty acid cycle and islet β-cell function in health, obesity and diabetes. Mol. Cell. Endocrinol. *353*, 88–100.
17. Randle, P.J., Garland, P.B., Hales, C.N., and Newsholme, E.A. (1963). The glucose fatty-acid cycle. Its role in insulin sensitivity and the metabolic disturbances of diabetes mellitus. Lancet *1*, 785–789.
18. Fang, Z., Weng, C., Li, H., Tao, R., Mai, W., Liu, X., Lu, L., Lai, S., Duan, Q., Alvarez, C., et al. (2019). Single-cell heterogeneity analysis and CRISPR screen identify key β-cell-specific disease genes. Cell Rep. *26*, 3132–3144.e7.
19. Skelin, M., Rupnik, M., and Cencic, A. (2010). Pancreatic beta cell lines and their applications in diabetes mellitus research. ALTEX *27*, 105–113.
20. Subramanian, A., Tamayo, P., Mootha, V.K., Mukherjee, S., Ebert, B.L., Gillette, M.A., Paulovich, A., Pomeroy, S.L., Golub, T.R., Lander, E.S., et al. (2005). Gene set enrichment analysis: a knowledge-based approach for interpreting genome-wide expression profiles. Proc. Natl. Acad. Sci. USA *102*, 15545–15550.
21. Vilar, S., Cozza, G., and Moro, S. (2008). Medicinal chemistry and the molecular operating environment (MOE): application of QSAR and molecular docking to drug discovery. Curr. Top. Med. Chem. *8*, 1555–1572.
22. de Leeuw, C.A., Mooij, J.M., Heskes, T., and Posthuma, D. (2015). MAGMA: generalized gene-set analysis of GWAS data. PLoS Comput. Biol. *11*, e1004219.
23. Tsoukalas, D., Fragoulakis, V., Sarandi, E., Docea, A.O., Papakonstaninou, E., Tsilimidos, G., Anamaterou, C., Fragkiadaki, P., Aschner, M., Tsatsakis, A., et al. (2019). Targeted metabolomic analysis of serum fatty acids for the prediction of autoimmune diseases. Front. Mol. Biosci. *6*, 120.
24. Mir, S.U.R., George, N.M., Zahoor, L., Harms, R., Guinn, Z., and Sarvetnick, N.E. (2015). Inhibition of autophagic turnover in β-cells by fatty acids and glucose leads to apoptotic cell death. J. Biol. Chem. *290*, 6071–6085.
25. Mogilenko, D.A., Haas, J.T., L'homme, L., Fleury, S., Quemener, S., Levavasseur, M., Becquart, C., Wartelle, J., Bogomolova, A., Pineau, L., et al. (2019). Metabolic and innate immune cues merge into a specific inflammatory response via the UPR. Cell *178*, 263.
26. Chen, X., Shang, L., Deng, S., Li, P., Chen, K., Gao, T., Zhang, X., Chen, Z., and Zeng, J. (2020). Peroxisomal oxidation of erucic acid suppresses mitochondrial fatty acid oxidation by stimulating malonyl-CoA formation in the rat liver. J. Biol. Chem. *295*, 10168–10179.
27. Ubellacker, J.M., Tasdogan, A., Ramesh, V., Shen, B., Mitchell, E.C., Martin-Sandoval, M.S., Gu, Z., McCormick, M.L., Durham, A.B., Spitz, D.R., et al. (2020). Lymph protects metastasizing melanoma cells from ferroptosis. Nature *585*, 113–118.
28. Lytrivi, M., Ghaddar, K., Lopes, M., Rosengren, V., Piron, A., Yi, X., Johansson, H., Lehtiö, J., Igoillo-Esteve, M., Cunha, D.A., et al. (2020). Combined transcriptome and proteome profiling of the pancreatic β-cell response to palmitate unveils key pathways of β-cell lipotoxicity. BMC Genomics *21*, 590.
29. Coleman, R.A., and Mashek, D.G. (2011). Mammalian triacylglycerol metabolism: synthesis, lipolysis, and signaling. Chem. Rev. *111*, 6359–6386.
30. Assimacopoulos-Jeannet, F., Thumelin, S., Roche, E., Esser, V., McGarry, J.D., and Prentki, M. (1997). Fatty acids rapidly induce the carnitine palmitoyltransferase I gene in the pancreatic β-cell line INS-1. J. Biol. Chem. *272*, 1659–1664.
31. Bray, M.-A., Singh, S., Han, H., Davis, C.T., Borgeson, B., Hartland, C., Kost-Alimova, M., Gustafsdottir, S.M., Gibson, C.C., and Carpenter, A.E. (2016). Cell Painting, a high-content image-based assay for morphological profiling using multiplexed fluorescent dyes. Nat. Protoc. *11*, 1757–1774.
32. Liberzon, A., Birger, C., Thorvaldsdóttir, H., Ghandi, M., Mesirov, J.P., and Tamayo, P. (2015). The Molecular Signatures Database (MSigDB) hallmark gene set collection. Cell Syst. *1*, 417–425.
33. Tonazzi, A., Giangregorio, N., Console, L., Palmieri, F., and Indiveri, C. (2021). The mitochondrial carnitine acyl-carnitine carrier (SLC25A20): molecular mechanisms of transport, role in redox sensing and interaction with drugs. Biomolecules *11*, 521. https://doi.org/10.3390/biom11040521.
34. Longo, N., Frigeni, M., and Pasquali, M. (2016). Carnitine transport and fatty acid oxidation. Biochim. Biophys. Acta *1863*, 2422–2435.
35. Schröder, M., and Kaufman, R.J. (2005). The mammalian unfolded protein response. Annu. Rev. Biochem. *74*, 739–789.
36. Hotamisligil, G.S. (2010). Endoplasmic reticulum stress and the inflammatory basis of metabolic disease. Cell *140*, 900–917.
37. Eguchi, K., Manabe, I., Oishi-Tanaka, Y., Ohsugi, M., Kono, N., Ogata, F., Yagi, N., Ohto, U., Kimoto, M., Miyake, K., et al. (2012). Saturated fatty acid and TLR signaling link β cell dysfunction and islet inflammation. Cell Metab. *15*, 518–533.
38. Donath, M.Y., Dalmas, É., Sauter, N.S., and Böni-Schnetzler, M. (2013). Inflammation in obesity and diabetes: islet dysfunction and therapeutic opportunity. Cell Metab. *17*, 860–872.
39. Abifadel, M., Varret, M., Rabès, J.-P., Allard, D., Ouguerram, K., Devillers, M., Cruaud, C., Benjannet, S., Wickham, L., Erlich, D., et al. (2003). Mutations in PCSK9 cause autosomal dominant hypercholesterolemia. Nat. Genet. *34*, 154–156.
40. Hobbs, H.H., Brown, M.S., and Goldstein, J.L. (1992). Molecular genetics of the LDL receptor gene in familial hypercholesterolemia. Hum. Mutat. *1*, 445–466.
41. Howe, V., Sharpe, L.J., Prabhu, A.V., and Brown, A.J. (2017). New insights into cellular cholesterol acquisition: promoter analysis of human HMGCR and SQLE, two key control enzymes in cholesterol synthesis. Biochim. Biophys. Acta Mol. Cell Biol. Lipids *1862*, 647–657.
42. Khoo, S., Gibson, T.B., Arnette, D., Lawrence, M., January, B., McGlynn, K., Vanderbilt, C.A., Griffen, S.C., German, M.S., and Cobb, M.H. (2004). MAP kinases and their roles in pancreatic beta-cells. Cell Biochem. Biophys. *40*, 191–200.
43. Dusaulcy, R., Handgraaf, S., Visentin, F., Howald, C., Dermitzakis, E.T., Philippe, J., and Gosmain, Y. (2019). High-fat diet impacts more changes in beta-cell compared to alpha-cell transcriptome. PLoS One *14*, e0213299.
44. Marmugi, A., Parnis, J., Chen, X., Carmichael, L., Hardy, J., Mannan, N., Marchetti, P., Piemonti, L., Bosco, D., Johnson, P., et al. (2016). Sorcin links pancreatic β-cell lipotoxicity to ER Ca2+ stores. Diabetes *65*, 1009–1021.
45. Fu, S., Yang, L., Li, P., Hofmann, O., Dicker, L., Hide, W., Lin, X., Watkins, S.M., Ivanov, A.R., and Hotamisligil, G.S. (2011). Aberrant lipid metabolism disrupts calcium homeostasis causing liver endoplasmic reticulum stress in obesity. Nature *473*, 528–531.
46. Orrenius, S., Zhivotovsky, B., and Nicotera, P. (2003). Regulation of cell death: the calcium–apoptosis link. Nat. Rev. Mol. Cell Biol. *4*, 552–565.
47. Sun, Y., Ge, X., Li, X., He, J., Wei, X., Du, J., Sun, J., Li, X., Xun, Z., Liu, W., et al. (2020). High-fat diet promotes renal injury by inducing oxidative stress and mitochondrial dysfunction. Cell Death Dis. *11*, 914.
48. Jang, H.-S., Noh, M.R., Kim, J., and Padanilam, B.J. (2020). Defective mitochondrial fatty acid oxidation and lipotoxicity in kidney diseases. Front. Med. *7*, 65.
49. Yin, F. (2023). Lipid metabolism and Alzheimer's disease: clinical evidence, mechanistic link and therapeutic promise. FEBS Journal *290*, 1420–1453. https://doi.org/10.1111/febs.16344.

50. Guttenplan, K.A., Weigel, M.K., Prakash, P., Wijewardhane, P.R., Hasel, P., Rufen-Blanchette, U., Münch, A.E., Blum, J.A., Fine, J., Neal, M.C., et al. (2021). Neurotoxic reactive astrocytes induce cell death via saturated lipids. Nature *599*, 102–107.

51. Ioannou, M.S., Jackson, J., Sheu, S.-H., Chang, C.-L., Weigel, A.V., Liu, H., Pasolli, H.A., Xu, C.S., Pang, S., Matthies, D., et al. (2019). Neuron-astrocyte metabolic coupling protects against activity-induced fatty acid toxicity. Cell *177*, 1522–1535.e14.

52. Tcw, J., Qian, L., Pipalia, N.H., Chao, M.J., Liang, S.A., Shi, Y., Jain, B.R., Bertelsen, S.E., Kapoor, M., Marcora, E., et al. (2022). Cholesterol and matrisome pathways dysregulated in astrocytes and microglia. Cell *185*, 2213–2233.e25.

53. Bachiller, S., Jiménez-Ferrer, I., Paulus, A., Yang, Y., Swanberg, M., Deierborg, T., and Boza-Serrano, A. (2018). Microglia in neurological diseases: a road map to brain-disease dependent-inflammatory response. Front. Cell. Neurosci. *12*, 488.

54. Plötz, T., von Hanstein, A.S., Krümmel, B., Laporte, A., Mehmeti, I., and Lenzen, S. (2019). Structure-toxicity relationships of saturated and unsaturated free fatty acids for elucidating the lipotoxic effects in human EndoC-βH1 beta-cells. Biochim. Biophys. Acta Mol. Basis Dis. *1865*, 165525.

55. Vogtmann, H., Christian, R., Hardin, R.T., and Clandinin, D.R. (1975). The effects of high and low erucic acid rapeseed oils in diets for rats. Int. J. Vitam. Nutr. Res. *45*, 221–229.

56. Oyadomari, S., and Mori, M. (2004). Roles of CHOP/GADD153 in endoplasmic reticulum stress. Cell Death Differ. *11*, 381–389.

57. Chan, J.Y., Luzuriaga, J., Maxwell, E.L., West, P.K., Bensellam, M., and Laybutt, D.R. (2015). The balance between adaptive and apoptotic unfolded protein responses regulates β-cell death under ER stress conditions through XBP1, CHOP and JNK. Mol. Cell. Endocrinol. *413*, 189–201.

58. Hotamisligil, G.S. (2017). Inflammation, metaflammation and immunometabolic disorders. Nature *542*, 177–185.

59. Hayden, M.S., and Ghosh, S. (2008). Shared principles in NF-kappaB signaling. Cell *132*, 344–362.

60. Oh, Y.S., Bae, G.D., Baek, D.J., Park, E.-Y., and Jun, H.-S. (2018). Fatty acid-induced lipotoxicity in pancreatic beta-cells during development of type 2 diabetes. Front. Endocrinol. *9*, 384.

61. Ebato, C., Uchida, T., Arakawa, M., Komatsu, M., Ueno, T., Komiya, K., Azuma, K., Hirose, T., Tanaka, K., Kominami, E., et al. (2008). Autophagy is important in islet homeostasis and compensatory increase of beta cell mass in response to high-fat diet. Cell Metab. *8*, 325–332.

62. Maxwell, K.G., and Millman, J.R. (2021). Applications of iPSC-derived beta cells from patients with diabetes. Cell Rep. Med. *2*, 100238.

63. Hogrebe, N.J., Augsornworawat, P., Maxwell, K.G., Velazco-Cruz, L., and Millman, J.R. (2020). Targeting the cytoskeleton to direct pancreatic differentiation of human pluripotent stem cells. Nat. Biotechnol. *38*, 460–470.

64. Olzmann, J.A., and Carvalho, P. (2019). Dynamics and functions of lipid droplets. Nat. Rev. Mol. Cell Biol. *20*, 137–155.

65. Promlek, T., Ishiwata-Kimata, Y., Shido, M., Sakuramoto, M., Kohno, K., and Kimata, Y. (2011). Membrane aberrancy and unfolded proteins activate the endoplasmic reticulum stress sensor Ire1 in different ways. Mol. Biol. Cell *22*, 3520–3532.

66. Volmer, R., van der Ploeg, K., and Ron, D. (2013). Membrane lipid saturation activates endoplasmic reticulum unfolded protein response transducers through their transmembrane domains. Proc. Natl. Acad. Sci. USA *110*, 4628–4633.

67. Shen, Y., Zhao, Z., Zhang, L., Shi, L., Shahriar, S., Chan, R.B., Di Paolo, G., and Min, W. (2017). Metabolic activity induces membrane phase separation in endoplasmic reticulum. Proc. Natl. Acad. Sci. USA *114*, 13394–13399.

68. Ho, N., Yap, W.S., Xu, J., Wu, H., Koh, J.H., Goh, W.W.B., George, B., Chong, S.C., Taubert, S., and Thibault, G. (2020). Stress sensor Ire1 deploys a divergent transcriptional program in response to lipid bilayer stress. J. Cell Biol. *219*, e201909165. https://doi.org/10.1083/jcb.201909165.

69. Golfetto, O., Hinde, E., and Gratton, E. (2013). Laurdan fluorescence lifetime discriminates cholesterol content from changes in fluidity in living cell membranes. Biophys. J. *104*, 1238–1247.

70. Pérez-Martí, A., Ramakrishnan, S., Li, J., Dugourd, A., Molenaar, M.R., De La Motte, L.R., Grand, K., Mansouri, A., Parisot, M., Lienkamp, S.S., et al. (2022). Reducing lipid bilayer stress by monounsaturated fatty acids protects renal proximal tubules in diabetes. eLife *11*, e74391. https://doi.org/10.7554/eLife.74391.

71. Ruiz, M., Ståhlman, M., Borén, J., and Pilon, M. (2019). AdipoR1 and AdipoR2 maintain membrane fluidity in most human cell types and independently of adiponectin. J. Lipid Res. *60*, 995–1004.

72. Ruiz, M., Devkota, R., Panagaki, D., Bergh, P.-O., Kaper, D., Henricsson, M., Nik, A., Petkevicius, K., Höög, J.L., Bohlooly-Y, M., et al. (2021). Sphingosine 1-phosphate mediates adiponectin receptor signaling essential for lipid homeostasis and embryogenesis. https://doi.org/10.1101/2021.08.12.456080.

73. Dempfle, A., Scherag, A., Hein, R., Beckmann, L., Chang-Claude, J., and Schäfer, H. (2008). Gene–environment interactions for complex traits: definitions, methodological requirements and challenges. Eur. J. Hum. Genet. *16*, 1164–1172.

74. Claussnitzer, M., Cho, J.H., Collins, R., Cox, N.J., Dermitzakis, E.T., Hurles, M.E., Kathiresan, S., Kenny, E.E., Lindgren, C.M., MacArthur, D.G., et al. (2020). A brief history of human disease genetics. Nature *577*, 179–189.

75. DIAbetes Genetics Replication And Meta-analysis (DIAGRAM) Consortium; Asian Genetic Epidemiology Network Type 2 Diabetes (AGEN-T2D) Consortium; South Asian Type 2 Diabetes (SAT2D) Consortium; Mexican American Type 2 Diabetes (MAT2D) Consortium; Type 2 Diabetes Genetic Exploration by Nex-generation sequencing in muylti-Ethnic Samples (T2D-GENES) Consortium, Mahajan, A., Go, M.J., Zhang, W., Below, J.E., Gaulton, K.J., et al. (2014). Genome-wide trans-ancestry meta-analysis provides insight into the genetic architecture of type 2 diabetes susceptibility. Nat. Genet. *46*, 234–244.

76. Fuchsberger, C., Flannick, J., Teslovich, T.M., Mahajan, A., Agarwala, V., Gaulton, K.J., Ma, C., Fontanillas, P., Moutsianas, L., McCarthy, D.J., et al. (2016). The genetic architecture of type 2 diabetes. Nature *536*, 41–47.

77. Flannick, J., Thorleifsson, G., Beer, N.L., Jacobs, S.B.R., Grarup, N., Burtt, N.P., Mahajan, A., Fuchsberger, C., Atzmon, G., Benediktsson, R., et al. (2014). Loss-of-function mutations in SLC30A8 protect against type 2 diabetes. Nat. Genet. *46*, 357–363.

78. Dwivedi, O.P., Lehtovirta, M., Hastoy, B., Chandra, V., Krentz, N.A.J., Kleiner, S., Jain, D., Richard, A.-M., Abaitua, F., Beer, N.L., et al. (2019). Loss of ZnT8 function protects against diabetes by enhanced insulin secretion. Nat. Genet. *51*, 1596–1606.

79. Thomsen, S.K., Raimondo, A., Hastoy, B., SenGupta, S., Dai, X.-Q., Bautista, A., Censin, J., Payne, A.J., Umapathysivam, M.M., Spigelman, A.F., et al. (2018). Type 2 diabetes risk alleles in PAM impact insulin release from human pancreatic β-cells. Nat. Genet. *50*, 1122–1131.

80. Mahajan, A., Taliun, D., Thurner, M., Robertson, N.R., Torres, J.M., Rayner, N.W., Payne, A.J., Steinthorsdottir, V., Scott, R.A., Grarup, N., et al. (2018). Fine-mapping type 2 diabetes loci to single-variant resolution using high-density imputation and islet-specific epigenome maps. Nat. Genet. *50*, 1505–1513.

81. Onengut-Gumuscu, S., Chen, W.-M., Burren, O., Cooper, N.J., Quinlan, A.R., Mychaleckyj, J.C., Farber, E., Bonnie, J.K., Szpak, M., Schofield, E., et al. (2015). Fine mapping of type 1 diabetes susceptibility loci and evidence for colocalization of causal variants with lymphoid gene enhancers. Nat. Genet. *47*, 381–386.

82. Schizophrenia Working Group of the Psychiatric; Genomics Consortium (2014). Biological insights from 108 schizophrenia-associated genetic loci. Nature *511*, 421–427.

83. Kataoka, K., Shioda, S., Ando, K., Sakagami, K., Handa, H., and Yasuda, K. (2004). Differentially expressed Maf family transcription factors, c-Maf and MafA, activate glucagon and insulin gene expression in pancreatic islet alpha- and beta-cells. J. Mol. Endocrinol. *32*, 9–20. https://doi.org/10.1677/jme.0.0320009.

84. Moktefi, A., Zhang, S.-Y., Vachin, P., Ory, V., Henique, C., Audard, V., Rucker-Martin, C., Gouadon, E., Eccles, M., Schedl, A., et al. (2016). Repression of CMIP transcription by WT1 is relevant to podocyte health. Kidney Int. *90*, 1298–1311.

85. Bouachi, K., Moktefi, A., Zhang, S.-Y., Oniszczuk, J., Sendeyo, K., Remy, P., Audard, V., Pawlak, A., Ollero, M., and Sahali, D. (2018). Expression of CMIP in podocytes is restricted to specific classes of lupus nephritis. PLoS One *13*, e0207066.

86. Zhang, J., Huang, J., Wang, X., Chen, W., Tang, Q., Fang, M., and Qian, Y. (2017). CMIP is oncogenic in human gastric cancer cells. Mol. Med. Rep. *16*, 7277–7286.

87. Cao, Y., Wang, T., Wu, Y., Juan, J., Qin, X., Tang, X., Wu, T., and Hu, Y. (2018). Opposite genetic effects of CMIP polymorphisms on the risk of type 2 diabetes and obesity: a family-based study in China. Int. J. Mol. Sci. *19*, 1011. https://doi.org/10.3390/ijms19041011.

88. Mo, M.-Q., Pan, L., Lu, Q.-M., Li, Q.-L., and Liao, Y.-H. (2018). The association of the CMIP rs16955379 polymorphism with dyslipidemia and the clinicopathological features of IgA nephropathy. Int. J. Clin. Exp. Pathol. *11*, 5008–5023.

89. Kamal, M., Valanciute, A., Dahan, K., Ory, V., Pawlak, A., Lang, P., Guellaen, G., and Sahali, D. (2009). C-mip interacts physically with RelA and inhibits nuclear factor kappa B activity. Mol. Immunol. *46*, 991–998.

90. Keaton, J.M., Gao, C., Guan, M., Hellwege, J.N., Palmer, N.D., Pankow, J.S., Fornage, M., Wilson, J.G., Correa, A., Rasmussen-Torvik, L.J., et al. (2018). Genome-wide interaction with the insulin secretion locus MTNR1B reveals CMIP as a novel type 2 diabetes susceptibility gene in African Americans. Genet. Epidemiol. *42*, 559–570.

91. Taneera, J., Lang, S., Sharma, A., Fadista, J., Zhou, Y., Ahlqvist, E., Jonsson, A., Lyssenko, V., Vikman, P., Hansson, O., et al. (2012). A systems genetics approach identifies genes and pathways for type 2 diabetes in human islets. Cell Metab. *16*, 122–134.

92. Kamal, M., Pawlak, A., BenMohamed, F., Valanciuté, A., Dahan, K., Candelier, M., Lang, P., Guellaën, G., and Sahali, D. (2010). C-mip interacts with the p85 subunit of PI3 kinase and exerts a dual effect on ERK signaling via the recruitment of Dip1 and DAP kinase. FEBS Lett. *584*, 500–506.

93. Camaya, I., Donnelly, S., and O'Brien, B. (2022). Targeting the PI3K/Akt signaling pathway in pancreatic β-cells to enhance their survival and function: an emerging therapeutic strategy for type 1 diabetes. J. Diabetes *14*, 247–260.

94. Elghazi, L., and Bernal-Mizrachi, E. (2009). Akt and PTEN: beta-cell mass and pancreas plasticity. Trends Endocrinol. Metab. *20*, 243–251.

95. Long, H.-Z., Cheng, Y., Zhou, Z.-W., Luo, H.-Y., Wen, D.-D., and Gao, L.-C. (2021). PI3K/AKT signal pathway: a target of natural products in the prevention and treatment of Alzheimer's disease and Parkinson's disease. Front. Pharmacol. *12*, 648636. https://doi.org/10.3389/fphar.2021.648636.

96. Wilding, J.P.H., Batterham, R.L., Calanna, S., Davies, M., Van Gaal, L.F., Lingvay, I., McGowan, B.M., Rosenstock, J., Tran, M.T.D., Wadden, T.A., et al. (2021). Once-weekly semaglutide in adults with overweight or obesity. N. Engl. J. Med. *384*, 989–1002.

97. Scott, R.A., Freitag, D.F., Li, L., Chu, A.Y., Surendran, P., Young, R., Grarup, N., Stancáková, A., Chen, Y., Varga, T.V., et al. (2016). A genomic approach to therapeutic target validation identifies a glucose-lowering GLP1R variant protective for coronary heart disease. Sci. Transl. Med. *8*, 341ra76.

98. Krentz, N.A.J., and Gloyn, A.L. (2020). Insights into pancreatic islet cell dysfunction from type 2 diabetes mellitus genetics. Nat. Rev. Endocrinol. *16*, 202–212.

99. Rayego-Mateos, S., Morgado-Pascual, J.L., Opazo-Ríos, L., Guerrero-Hue, M., García-Caballero, C., Vázquez-Carballo, C., Mas, S., Sanz, A.B., Herencia, C., Mezzano, S., et al. (2020). Pathogenic pathways and therapeutic approaches targeting inflammation in diabetic nephropathy. Int. J. Mol. Sci. *21*, 3798.

100. Sidhom, E.-H., Kim, C., Kost-Alimova, M., Ting, M.T., Keller, K., Avila-Pacheco, J., Watts, A.J., Vernon, K.A., Marshall, J.L., Reyes-Bricio, E., et al. (2021). Targeting a Braf/Mapk pathway rescues podocyte lipid peroxidation in CoQ-deficiency kidney disease. J. Clin. Invest. *131*, e141380. https://doi.org/10.1172/JCI141380.

101. Durán, A.M., Salto, L.M., Câmara, J., Basu, A., Paquien, I., Beeson, W.L., Firek, A., Cordero-MacIntyre, Z., and De León, M. (2019). Effects of omega-3 polyunsaturated fatty-acid supplementation on neuropathic pain symptoms and sphingosine levels in Mexican-Americans with type 2 diabetes. Diabetes Metab. Syndr. Obes. *12*, 109–120.

102. Munir, R., Lisec, J., Swinnen, J.V., and Zaidi, N. (2019). Lipid metabolism in cancer cells under metabolic stress. Br. J. Cancer *120*, 1090–1098.

103. Ringel, A.E., Drijvers, J.M., Baker, G.J., Catozzi, A., García-Cañaveras, J.C., Gassaway, B.M., Miller, B.C., Juneja, V.R., Nguyen, T.H., Joshi, S., et al. (2020). Obesity shapes metabolism in the tumor microenvironment to suppress anti-tumor immunity. Cell *183*, 1848–1866.e26.

104. Liangpunsakul, S., and Chalasani, N. (2019). Lipid mediators of liver injury in nonalcoholic fatty liver disease. Am. J. Physiol. Gastrointest. Liver Physiol. *316*, G75–G81.

105. de la Monte, S.M., and Tong, M. (2014). Brain metabolic dysfunction at the core of Alzheimer's disease. Biochem. Pharmacol. *88*, 548–559.

106. Cutuli, D., Landolfo, E., Nobili, A., De Bartolo, P., Sacchetti, S., Chirico, D., Marini, F., Pieroni, L., Ronci, M., D'Amelio, M., et al. (2020). Behavioral, neuromorphological, and neurobiochemical effects induced by omega-3 fatty acids following basal forebrain cholinergic depletion in aged mice. Alzheimers Res. Ther. *12*, 150. https://doi.org/10.1186/s13195-020-00705-3.

107. Desale, S.E., and Chinnathambi, S. (2020). Role of dietary fatty acids in microglial polarization in Alzheimer's disease. J. Neuroinflammation *17*, 93. https://doi.org/10.1186/s12974-020-01742-3.

108. Chausse, B., Kakimoto, P.A., Caldeira-da-Silva, C.C., Chaves-Filho, A.B., Yoshinaga, M.Y., da Silva, R.P., Miyamoto, S., and Kowaltowski, A.J. (2019). Distinct metabolic patterns during microglial remodeling by oleate and palmitate. Biosci. Rep. *39*, BSR20190072. https://doi.org/10.1042/BSR20190072.

109. Madore, C., Leyrolle, Q., Morel, L., Rossitto, M., Greenhalgh, A.D., Delpech, J.C., Martinat, M., Bosch-Bouju, C., Bourel, J., Rani, B., et al. (2020). Essential omega-3 fatty acids tune microglial phagocytosis of synaptic elements in the mouse developing brain. Nat. Commun. *11*, 6133. https://doi.org/10.1038/s41467-020-19861-z.

110. Snowden, S.G., Ebshiana, A.A., Hye, A., An, Y., Pletnikova, O., O'Brien, R., Troncoso, J., Legido-Quigley, C., and Thambisetty, M. (2017). Association between fatty acid metabolism in the brain and Alzheimer disease neuropathology and cognitive performance: a nontargeted metabolomic study. PLoS Med. *14*, e1002266.

111. Yoon, H., Shaw, J.L., Haigis, M.C., and Greka, A. (2021). Lipid metabolism in sickness and in health: emerging regulators of lipotoxicity. Mol. Cell *81*, 3708–3730.

112. German, N.J., Yoon, H., Yusuf, R.Z., Murphy, J.P., Finley, L.W.S., Laurent, G., Haas, W., Satterstrom, F.K., Guarnerio, J., Zaganjor, E., et al. (2016). PHD3 loss in cancer enables metabolic reliance on fatty acid oxidation via deactivation of ACC2. Mol. Cell *63*, 1006–1020.

113. Nakamura, M., Liu, T., Husain, S., Zhai, P., Warren, J.S., Hsu, C.P., Matsuda, T., Phiel, C.J., Cox, J.E., Tian, B., et al. (2019). Glycogen synthase kinase-3α promotes fatty acid uptake and lipotoxic cardiomyopathy. Cell Metab. *29*, 1119–1134.e12.

114. Dvela-Levitt, M., Kost-Alimova, M., Emani, M., Kohnert, E., Thompson, R., Sidhom, E.H., Rivadeneira, A., Sahakian, N., Roignot, J., Papagregoriou, G., et al. (2019). Small molecule targets TMED9 and promotes lysosomal degradation to reverse proteinopathy. Cell *178*, 521–535.e23.

115. Kamentsky, L., Jones, T.R., Fraser, A., Bray, M.A., Logan, D.J., Madden, K.L., Ljosa, V., Rueden, C., Eliceiri, K.W., and Carpenter, A.E. (2011). Improved structure, function and compatibility for CellProfiler: modular high-throughput image analysis software. Bioinformatics *27*, 1179–1180. https://doi.org/10.1093/bioinformatics/btr095.

116. Dao, D., Fraser, A.N., Hung, J., Ljosa, V., Singh, S., and Carpenter, A.E. (2016). CellProfiler Analyst: interactive data exploration, analysis and classification of large biological image sets. Bioinformatics *32*, 3210–3212. https://doi.org/10.1093/bioinformatics/btw390.

117. Köhler, N., Rose, T.D., Falk, L., and Pauling, J.K. (2021). Investigating global lipidome alterations with the lipid network explorer. Metabolites *11*, 488. https://doi.org/10.3390/metabo11080488.

118. Dobin, A., Davis, C.A., Schlesinger, F., Drenkow, J., Zaleski, C., Jha, S., Batut, P., Chaisson, M., and Gingeras, T.R. (2013). STAR: ultrafast universal RNA-seq aligner. Bioinformatics *29*, 15–21. https://doi.org/10.1093/bioinformatics/bts635.

119. DeLuca, D.S., Levin, J.Z., Sivachenko, A., Fennell, T., Nazaire, M.D., Williams, C., Reich, M., Winckler, W., and Getz, G. (2012). RNA-SeQC: RNA-seq metrics for quality control and process optimization. Bioinformatics *28*, 1530–1532. https://doi.org/10.1093/bioinformatics/bts196.

120. Liberzon, A., Subramanian, A., Pinchback, R., Thorvaldsdóttir, H., Tamayo, P., and Mesirov, J.P. (2011). Molecular signatures database (MSigDB) 3.0. Bioinformatics *27*, 1739–1740.

121. Mohamed, A., Molendijk, J., and Hill, M.M. (2020). lipidr: a software tool for data mining and analysis of lipidomics datasets. J. Proteome Res. *19*, 2890–2897.

122. Love, M.I., Huber, W., and Anders, S. (2014). Moderated estimation of fold change and dispersion for RNA-seq data with DESeq2. Genome Biol. *15*, 550. https://doi.org/10.1186/s13059-014-0550-8.

123. Leek, J.T., Johnson, W.E., Parker, H.S., Jaffe, A.E., and Storey, J.D. (2012). The sva package for removing batch effects and other unwanted variation in high-throughput experiments. Bioinformatics *28*, 882–883.

124. Langfelder, P., Zhang, B., and Horvath, S. (2008). Defining clusters from a hierarchical cluster tree: the Dynamic Tree Cut package for R. Bioinformatics *24*, 719–720.

125. Cahill, K.M., Huo, Z., Tseng, G.C., Logan, R.W., and Seney, M.L. (2018). Improved identification of concordant and discordant gene expression signatures using an updated rank-rank hypergeometric overlap approach. Sci. Rep. *8*, 9588.

126. Breiman, L. (2001). Random forests. Mach. Learn. *45*, 5–32.

127. Anders, S., Pyl, P.T., and Huber, W. (2015). HTSeq–a Python framework to work with high-throughput sequencing data. Bioinformatics *31*, 166–169.

128. Burns, S.M., Vetere, A., Walpita, D., Dančík, V., Khodier, C., Perez, J., Clemons, P.A., Wagner, B.K., and Altshuler, D. (2015). High-throughput luminescent reporter of insulin secretion for discovering regulators of pancreatic beta-cell function. Cell Metab. *21*, 126–137. https://doi.org/10.1016/j.cmet.2014.12.010.

129. Parnaud, G., Bosco, D., Berney, T., Pattou, F., Kerr-Conte, J., Donath, M.Y., Bruun, C., Mandrup-Poulsen, T., Billestrup, N., and Halban, P.A. (2008). Proliferation of sorted human and rat beta cells. Diabetologia *51*, 91–100.

130. Abud, E.M., Ramirez, R.N., Martinez, E.S., Healy, L.M., Nguyen, C.H.H., Newman, S.A., Yeromin, A.V., Scarfone, V.M., Marsh, S.E., Fimbres, C., et al. (2017). iPSC-derived human microglia-like cells to study neurological diseases. Neuron *94*, 278–293.e9.

131. Dolan, M.-J., Therrien, M., Jereb, S., Kamath, T., Atkeson, T., Marsh, S.E., Goeva, A., Lojek, N.M., Murphy, S., White, C.M., et al. (2022). A resource for generating and manipulating human microglial states in vitro. https://doi.org/10.1101/2022.05.02.490100.

132. Paynter, N.P., Balasubramanian, R., Giulianini, F., Wang, D.D., Tinker, L.F., Gopal, S., Deik, A.A., Bullock, K., Pierce, K.A., Scott, J., et al. (2018). Metabolic predictors of incident coronary heart disease in women. Circulation *137*, 841–853.

133. Narváez-Rivas, M., and Zhang, Q. (2016). Comprehensive untargeted lipidomic analysis using core-shell C30 particle column and high field Orbitrap mass spectrometer. J. Chromatogr. A *1440*, 123–134.

134. Picelli, S., Faridani, O.R., Björklund, A.K., Winberg, G., Sagasser, S., and Sandberg, R. (2014). Full-length RNA-seq from single cells using Smart-seq2. Nat. Protoc. *9*, 171–181.

135. Bray, M.-A., Fraser, A.N., Hasaka, T.P., and Carpenter, A.E. (2012). Workflow and metrics for image quality control in large-scale high-content screens. J. Biomol. Screen. *17*, 266–274.

136. Harris, F.M., Best, K.B., and Bell, J.D. (2002). Use of laurdan fluorescence intensity and polarization to distinguish between changes in membrane fluidity and phospholipid order. Biochim. Biophys. Acta *1565*, 123–128.

137. Parasassi, T., De Stasio, G., Ravagnan, G., Rusch, R.M., and Gratton, E. (1991). Quantitation of lipid phases in phospholipid vesicles by the generalized polarization of laurdan fluorescence. Biophys. J. *60*, 179–189.

138. Brown, M.R., Holmes, H., Rakshit, K., Javeed, N., Her, T.K., Stiller, A.A., Sen, S., Shull, G.E., Prakash, Y.S., Romero, M.F., et al. (2021). Electrogenic sodium bicarbonate cotransporter NBCe1 regulates pancreatic β cell function in type 2 diabetes. J. Clin. Invest. *131*, e142365. https://doi.org/10.1172/JCI142365.

STAR★METHODS

KEY RESOURCES TABLE

REAGENT or RESOURCE	SOURCE	IDENTIFIER
Antibodies		
Mouse monoclonal anti-CPT1A	Abcam	Cat#ab128568
Rabbit monoclonal anti-ATF4	Cell Signaling Technology	Cat#11815
Mouse monoclonal anti-CHOP	Cell Signaling Technology	Cat#2895
Rabbit polyclonal anti-CMIP	Novus Bio	NBP2-58180
Rabbit polyclonal anti-Akt	Cell Signaling Technology	Cat#9272
Rabbit monoclonal anti-pAkt	Cell Signaling Technology	Cat#4060
Rabbit polyclonal anti-AMPKα	Cell Signaling Technology	Cat#2532
Rabbit monoclonal anti-pAMPKα	Cell Signaling Technology	Cat#2535
Rabbit monoclonal anti-FOXO1	Cell Signaling Technology	Cat#2880
Rabbit polyclonal anti-pFOXO1	Cell Signaling Technology	Cat#9464
Rabbit monoclonal anti-GAPDH-HRP	Cell Signaling Technology	Cat#3683
Goat anti-rabbit IgG-HRP	Cell Signaling Technology	Cat#7074
Horse anti-mouse IgG-HRP	Cell Signaling Technology	Cat#7076
Rabbit polyclonal anti-CMIP	Proteintech	12851-1-AP
Rabbit IgG control	Thermo Fisher	10500C
Rabbit polyclonal anti-PI3K p85α	Cell Signaling Technology	Cat#4292
Rabbit monoclonal anti-NF-κB p65/RELA	Cell Signaling Technology	Cat#8242
Alexa Fluor 568 goat anti-rabbit IgG	Thermo Fisher Scientific	Cat#A11036
Rabbit monoclonal anti-Lc3b	Cell Signaling Technology	Cat#3868
Alexa Fluor 568 donkey anti-rabbit IgG	Thermo Fisher Scientific	Cat#A10042
Rat monoclonal anti-c-peptide	Developmental Studies Hybridoma Bank at the University of Iowa	GN-ID4
Alexa Fluor 568 goat anti-rat IgG	Life technologies	A11077
Bacterial and virus strains		
Cmip-specific sgRNA expressing E. coli	Millipore Sigma	Clone MM5000005403
Non-targeting control sgRNA expressing E. coli	Millipore Sigma	CRISPR20-1EA
Custom lentivirus with mouse *Cmip* ORF (NM_001163262.1) under CMV promoter, neomycin resistance	VectorBuilder	VB210401-1180uxy
Custom lentivirus with AA 2-83 of E. coli beta-galactosidase under CMV promoter, neomycin resistance	VectorBuilder	VB900122-0486zjw
Biological samples		
Cadaveric human islets	Integrated Islet Distribution Program	N/A
Chemicals, peptides, and recombinant proteins		
Laurdan (6-dodecanoyl-2-dimethylaminoaphthalene) dye	Thermo Fisher	D250
Fluo4	Life Technologies	Cat#F14202
Thapsigargin	Millipore Sigma	T9033; CAS 67526-95-8
Hoechst	Thermo Fisher Scientific	Cat#H3570
Rapamycin	Sigma-Aldrich	R8781
Bafilomycin A1	Sigma-Aldrich	SML1661
Alexa 647-conjugated phalloidin	Thermo Fisher Scientific	Cat#A22287
Pierce Protein A/G Magnetic Beads	Thermo Fisher	88802

(*Continued on next page*)

Continued

REAGENT or RESOURCE	SOURCE	IDENTIFIER
Propidium iodide	Thermo Fisher Scientific	Cat#P3566
Caspase 3/7	Thermo Fisher Scientific	Cat#C10423
Polybrene	Sigma	TR-1003-G
FuGENE	Promega	E2311
Essential 8 medium	Thermo Fisher Scientific	A1517001
Matrigel	Corning	07181
Accutase	Stem Cell Technologies	Cat#07920
Y27632 ROCK inhibitor	Selleckchem	S1049; CAS 129830-38-2
IMDM	Thermo Fisher Scientific	12440053
ITS-X	Thermo Fisher Scientific	51500056
L-ascorbic acid 2-Phosphate	Sigma	A8960; CAS 1713265-25-8
Monothioglycerol	Sigma	M6145; CAS 96-27-5
Poly(vinyl) alcohol (PVA)	Sigma	341584; CAS 9002-89-5
Chemically-defined lipid concentrate	Thermo Fisher Scientific	11905031
Non-essential amino acids	Thermo Fisher Scientific	11140050
FGF2	Thermo Fisher Scientific	100-18B-1MG
BMP4	Thermo Fisher Scientific	120-05-50UG
Activin-A	Thermo Fisher Scientific	120-14E-100UG
LiCL	Sigma	310468; CAS 7447-41-8
VEGF	PeproTech	100-20
TPO	PeproTech	300-18
SCF	Thermo Fisher Scientific	300-07-50UG
IL6	PeproTech	200-06
IL3	PeproTech	200-03
ITS-G	Thermo Fisher Scientific	41400045
B-27	Thermo Fisher Scientific	17504044
N2	Thermo Fisher Scientific	17502001
M-CSF	PeproTech	300-25
IL-34	PeproTech	200-34
TGFB-1	PeproTech	100-21
CD200	VWR	75790-456
CX3CL1	PeproTech	300-31
TCL buffer	Qiagen	Cat#1031576
Revitacell	Thermo Fisher Scientific	A2644501
CHIR99021	Stem Cell Technologies	72052
KGF	Lifeline Cell Technology	LS-1059
LDN193189	Stem Cell Technologies	72147
SANT1	Stem Cell Technologies	100-0538
TPPB	Tocris	5343; 497259-23-1
RA	Sigma Aldrich	R2625; CAS 302-79-4
Alk5i II	Sigma Aldrich	616452; CAS 446859-33-2
T3	Lifeline Cell Technology	LS-1044
Betacellulin	Peprotech	100-50
Latrunculin A	Thermo Fisher Scientific	L12370
Enzo SCREEN-WELL Fatty Acid library	Nuchek Prep	Cat#BML-2803-0100
Fatty acid free bovine serum albumin (BSA)	Sigma	Cat#A8806
RenaLife Renal Basal medium with RenaLife LifeFactors	Lifeline Cell Technology	LL-0025
HBSS with calcium	Thermo Fisher Scientific	Cat#14025076

(*Continued on next page*)

Continued

REAGENT or RESOURCE	SOURCE	IDENTIFIER
Critical commercial assays		
Mouse insulin ELISA	Thermo Fisher	EMINS
Agencourt RNA cleanup XP	Beckman Coulter	Cat#A63987
AMPure XP Agencourt	Beckman Coulter	Cat#100609
Qubit dsDNA High Sensitivity	Life Technologies	Cat#102689
Nextera XT DNA Library Preparation Kit	Illumina	Cat#FC-131-1096
Nextera XT Index Kit	Illumina	Cat#FC-131-1001
Bioanalyzer High Sensitivity DNA Kit	Agilent	Cat#5067-4627
NextSeq 75 cycle v2 kit	Illumina	Cat#TG-160-2002
Deposited data		
Bulk RNAseq data	This paper	GEO: GSE226911
Experimental models: Cell lines		
iPSC-microglia line	NIGMS Human Genetic Cell Repository at the Coriell Institute for Medical Research	AICS-0036-006
MIN6	Addex Bio	Cat#C0018008; RRID: CVCL_0431
INS-1E	University of Geneva, Switzerland	RRID: CVCL_0351
Immortalized human kidney epithelial cells	Dvela-Levitt et al.[114]	WFUHS IRB00014033
iPSC-beta cell line	Gibco	Cat#A18945
Oligonucleotides		
CMIP-specific sgRNA; ACGTCTTC AATGGCGCTGTAGG	This paper	N/A
Non-targeting sgRNA; GTATTACT GATATTGGTGGG	This paper	N/A
3'RT; AGCAGTGGTATCAACGCA GAGTAC(T30)VN	Integrated DNA Technologies	N/A
Template switching; AAGCAG TGGTATCAACGCAGAGTA CrGrG+G	Qiagen	N/A
ISPCR; AAGCAGTGGTATCAA CGCAGAGT	Integrated DNA Technologies	N/A
Software and algorithms		
MAGMA (v 1.07)	de Leeuw et al.[22]	https://ctg.cncr.nl/software/magma
Molecular Operating Environment (MOE)	Chemical Computing Group	N/A
CellProfiler 2.2.0	Kamentsky et al.[115]	https://cellprofiler.org/
CellProfiler Analyst	Bray et al.[31]; Dao et al.[116]	https://cellprofileranalyst.org/
Cytominer	Bray et al.[31]	https://github.com/cytomining/cytominer
LipidSearch version 5.0 SP	Thermo Fisher Scientific	https://www.thermofisher.com/us/en/home/industrial/mass-spectrometry/liquid-chromatography-mass-spectrometry-lc-ms/lc-ms-software/multi-omics-data-analysis/lipid-search-software.html
TraceFinder 3.3	Thermo Fisher Scientific	OPTON-31006
Progenesis QI	Nonlinear Dynamics	https://www.nonlinear.com/progenesis/qi/
Lipid Network Explorer	Köhler et al.[117]	https://exbio.wzw.tum.de/linex/
Spliced Transcript Alignment to a Reference (STAR)	Dobin et al.[118]	http://code.google.com/p/rna-star/
RNA-SeQC	DeLuca et al.[119]	https://software.broadinstitute.org/cancer/cga/rna-seqc

(*Continued on next page*)

Continued

REAGENT or RESOURCE	SOURCE	IDENTIFIER
Gene Set Enrichment Analysis (GSEA); Molecular Signatures Database (MSigDB)	Subramanian et al.[20]; Liberzon et al.[120]	https://www.gsea-msigdb.org/gsea/msigdb/
MATLAB 2020a	MathWorks	https://www.mathworks.com/products/matlab.html
Cytoscape	N/A	https://cytoscape.org/
R; packages: lipidR, DESeq2, surrogate variable analysis (SVA), RRHO2, WGCNA, randomforest	Mohamed et al.[121]; Love et al.[122]; Leek et al.[123]; Langfelder et al.[124]; Cahill et al.[125]; Breiman[126]	https://www.r-project.org/
Python; packages: HTSeq	Anders et al.[127]	https://www.python.org/
Other		
Opera Phenix High Content Screening System	Perkin Elmer	Cat#HH14000000
384-well Cell Carrier Ultra plate	Perkin Elmer	Cat#6057300
96-well Cell Carrier Ultra plate	Perkin Elmer	Cat#6055308

RESOURCE AVAILABILITY

Lead Contact

Further information and requests for resources and reagents should be directed to and will be fulfilled by the lead contact, Anna Greka (agreka@bwh.harvard.edu).

Materials Availability

This study did not generate new unique reagents.

Data and code availability

Bulk RNA-seq data have been deposited at GEO and are publicly available as of the date of publication. Accession numbers are listed in the key resources table. Original western blot images are available from the lead contact upon request.

This paper does not report original code.

Any additional information required to reanalyze the data reported in this paper is available from the lead contact upon request.

EXPERIMENTAL MODEL AND SUBJECT DETAILS

Cell lines

MIN6 cells were purchased (Addex Bio, #C0018008, SV40 T-antigen induced cell immortalization of C57BL/6 IT6 transgenic mus musculus insulinoma, sex unspecified) and cultured as described previously.[128] In short, cells were maintained in DMEM with 4.5 g/L glucose, supplemented with 10% FBS (fetal bovine serum, Life Technologies, #26140079), 100 U/ml penicillin and 100 μg/ml streptomycin (#15140 Invitrogen) and 55 μM beta-mercaptoethanol (Sigma, #M6250). MIN6 cells were cultured at 37°C with 5% CO2 and used for experiments up to passage 30.

Immortalized human kidney epithelial cells used in this study were generated with informed consent under WFUHS IRB00014033.[114] Cells extracted from the kidney of a healthy female human donor were immortalized using lentivirus carrying human Telomerase Reverse Transcriptase (hTERT). They were maintained at 37°C with 5% CO2 in RenaLife Renal Basal Medium supplemented with RenaLife LifeFactors (Lifeline Cell Technology), with the exclusion of gentamicin and amphotericin B.

INS-1E cells (University of Geneva, Rattus norvegicus NEDH, male) were grown at 37°C with 5% CO2 in RPMI 1640 media, supplemented with 10% FBS, 1% penicillin and streptomycin, 1% sodium pyruvate, and 50 μM β-mercaptoethanol (all from Life Technologies). Cells were maintained in flasks pre-coated with supernatant from rat 804G cell line (804G matrix) as previously described.[129]

Cell lines were routinely checked and were negative for mycoplasma.

iPSC-derived cells

The iPSC-derived beta cells were differentiated as described previously[62,63] from an episomal reprogrammed iPSC line (Gibco, #A18945). The factors added each day of differentiation can be found in Table S7. After the conclusion of the 28 day differentiation process, these cells were maintained in enriched serum-free media (ESFM) with media changes every other day. On day 30, the cultures were dissociated with TrypLE incubation for a maximum of 5 min, followed by neutralization with ESFM, TrypLE removal through centrifugation at 200xg for 3 min, filtration through a 40 μm filter to remove large clumps, and seeding onto HTB-9 ECM coated 96-well plates (Perkin Elmer, CellCarrier Ultra, #6055308) at 10,000/well.

AICS-0036-006 from the NIGMS Human Genetic Cell Repository at the Coriell Institute for Medical Research was used to generate the microglia in this study. iPSCs were cultured in Essential 8 (E8) (Thermo Fisher Scientific) media on Matrigel (Corning) coated 6-well plates. Media was changed daily until confluence. iMGLs were differentiated as previously described.[130,131] When confluent, iPSCs were dissociated using Accutase (Stem Cell technologies), centrifuged for 5 mins at 300xg and counted using trypan blue (Thermo Fisher Scientific). 200,000 cells/well were resuspended in E8 containing 10 μM Y27632 ROCK inhibitor (Selleckchem) in low adherence 6-well plates (Corning). For the first 10 days, cells were cultured in HPC medium [50% IMDM (Thermo Fisher Scientific), 50% F12 (Thermo Fisher Scientific), ITS-X 2% v/v (Thermo Fisher Scientific), L-ascorbic acid 2-Phosphate (64 ug/ml, Sigma), monothioglycerol (400mM, Sigma), Poly(vinyl) alcohol (PVA) (10mg/ml, Sigma), Glutamax (1X, Thermo Fisher Scientific), chemically-defined lipid concentrate (1X, Thermo Fisher Scientific) and non-essential amino acids (Thermo Fisher Scientific)]. At day 0, embryoid bodies (EB) were gently collected, centrifuged at 100xg and resuspended in HPC medium supplemented with 1 μM ROCK inhibitor, FGF2 (50 ng/ml, Thermo Fisher Scientific), BMP4 (50ng/ml, Thermo Fisher Scientific), Activin-A (12.5ng/ml, Thermo Fisher Scientific) and LiCL (2 mM, Sigma), then incubated in a hypoxic incubator (5% O2, 5% CO2, 37℃). On day 2, cells were gently collected and the media changed to HPC medium supplemented with FGF2 (50ng/ml, Thermo Fisher Scientific) and VEGF (50 ng/ml, PeproTech) and returned to the hypoxic incubator. On day 4, cells were collected and media changed to HPC medium supplemented with FGF2 (50ng/ml, Thermo Fisher Scientific), VEGF (50 ng/ml, PeproTech), TPO (50 ng/ml, PeproTech), SCF (10ng/ml, Thermo Fisher Scientific), IL6 (50ng/ml, PeproTech) and IL3 (10ng/ml, PeproTech) and incubated in a normoxic incubator (20% O2, 5% CO2, 37C). At day 6 and 8, 1 ml of day 4 media was added in each well. On day 10, cells were collected, counted using trypan blue and frozen in Cryostor (Sigma Aldrich) in aliquots of 300,000-500,000 cells.

For iMGL differentiation, cells were thawed, washed 1x with PBS and plated at 200,000 cells per well in 6-well plates coated with matrigel in iMGL media [DMEM/F12 (Thermo Fisher Scientific), ITS-G (2% v/v, Thermo Fisher Scientific), B27 (2% v/v, Thermo Fisher Scientific), N2 (0.5% v/v, Thermo Fisher Scientific), monothioglycerol (200 mM, Sigma), Glutamax (1X, Thermo Fisher Scientific), non-essential amino acids (1X, Thermo Fisher Scientific)] supplemented with M-CSF (25 ng/ml, PeproTech), IL-34 (10 ng/ml, PeproTech) and TGFB-1 (50ng/ml, PeproTech). Cells were fed every 2 days and replated at day 22. On day 30, cells were collected and replated in iMGL media supplemented with M-CSF (25 ng/ml, PeproTech), IL-34 (10 ng/ml, PeproTech), TGFB-1 (50ng/ml, PeproTech), CD200 (100ng/ml, VWR) and CX3CL1 (100ng/ml, PeproTech).

Primary cells

Primary human islets from three independent non-diabetic cadaveric donors were received from the Integrated Islet Distribution Program. These islets were from 2 females and one male with ages ranging from 31-54 years, BMI 24.5-27.4, greater than 90% purity, and greater than 95% viability. Intact islets were dissociated using accutase followed by trituration and stained using Trypan Blue to confirm viability. They were seeded at 15,000/well into 384-well Cell Carrier Ultra microplates (Perkin Elmer, CellCarrier Ultra, #6057300) coated with HTB-9-derived ECM and maintained with CMRL 1066 medium (CellGro, 15-110-CV) supplemented with 10% FBS, 1× L-glutamine, and 1× penicillin/streptomycin.

METHOD DETAILS

FFA Preparation

Enzo SCREEN-WELL Fatty Acid library (#BML-2803-0100) containing FFAs dissolved in DMSO ($[FFA]_{stock}$ = 10 μM) was stored in glass vials at -20°C in the compound management facility of the Broad Institute. Template plates for High Throughput Screens were stored up to 4 weeks at 4°C. To prepare compound plates, small volumes of DMSO dissolved FFAs were transferred into microplates containing fatty acid free BSA (Sigma #A8806) solutions in ddH_2O in a molecular ratio of 1:6.67 (BSA:FFA, $[FFA]_{final}$ = 500 μM) with an automated simultaneous pipettor (Analytik Jena CyBio Well Vario). Plates were incubated overnight for 24 h at 37 °C to ensure complete binding of FFAs to BSA. Next, DMSO and ddH_2O were completely removed with the GeneVac HT-12 evaporator for 12 h with full vacuum at 37 °C and continuous centrifugation at 400g. Plates with dry FFA bound BSA crystals in the wells were resuspended in MIN6 culture medium at room temperature for 4-8 h on an orbital plate shaker. After resuspension, compound plates were spun down at 5000g for 10 min and manually transferred to 384 MultiScreenHTS HV Filter Plates (0.45 μm, Millipore, #MZHVN0W10) and spun down again for 1 min at 500g into an empty compound plate. Resulting filtered compound plates were transferred into assay plates of the same format as the CyBio Well Vario simultaneous pipettor. Representative FFAs were ordered from Nu-Chek Prep, manually dissolved in DMSO ($[FFA]_{stock}$ = 10 μM) and prepared in glass vials according to the same protocol.

Differential Scanning Calorimetry

All differential scanning calorimetry (DSC) measurements were performed with a MicroCal VP-Capillary DSC Automated system (Malvern Panalytical). Selected FFAs were bound to BSA in microplates according to the protocol described above and resuspended in PBS to a final concentration of $[BSA]_{final}$ = 50 μM. Sample measurements included one measurement of PBS vs. PBS to record a baseline reference curve at the scan rate of 200 °C/h. The samples were heated from T_{start} = 10 °C up to T_{end} = 90 °C at the same scan rate. The melting temperature T_m was determined from the resulting single-peak melting curve using FFA-free BSA as a control.

Lipid Profiling

40,000 MIN6 cells/well were seeded in 96 well plates 24 h prior to treatment in three replicates. FFA library compound plates were transferred into assay plates which were then incubated for 24 h. The lipid fraction of cells was isolated with isopropanol after washing the plates 3 times with ice cold PBS. After the addition of isopropanol, plates were incubated for 1 h at 4 °C. IPA extracts were then manually transferred to autosampler vials (Waters), capped, and stored at -80 °C until analysis. Lipid profiling was done as previously described.[132] Briefly, non-targeted liquid chromatography mass spectrometry (LC-MS) data were acquired using a system composed of a Nexera X2 U-HPLC system (Shimadzu Scientific Instruments; Marlborough, MA) coupled to a Q Exactive Focus Orbitrap mass spectrometer (Thermo Fisher Scientific; Waltham, MA). Cell extracts (2 μL) were injected directly onto a 100 x 2.1 mm, 1.7 μm ACQUITY BEH C8 column (Waters; Milford, MA). The column was then eluted isocratically with 80% mobile phase A (95/5/0.1; vol/vol/vol 10mM ammonium acetate/methanol/formic acid) for 1 min followed by a linear gradient to 80% mobile-phase B (99.9/0.1; vol/vol methanol/formic acid) over 2 min, a linear gradient to 100% mobile phase B over 7 min, then 3 min at 100% mobile-phase B. Mass spectrometry analyses were carried out using ESI in the positive ion mode using full scan analysis over 220–1100 m/z. Raw data were processed and visually inspected using TraceFinder 3.3 software (Thermo Fisher Scientific; Waltham, MA) and Progenesis QI (Nonlinear Dynamics; Newcastle upon Tyne, UK). The identity of individual metabolites and lipid families was confirmed by matching their retention time to that of authentic reference standards.

For the comparison between the PA and EA-induced lipidomes, MIN6 were seeded at 800,000 per well in a 6-well plate and grown for 3 days (n=4). After the cells were treated with the respective FFAs at 500 μM for 24h, cells were washed 3x with 1ml of room temperature PBS. Cells were scraped in 500ul room temperature PBS, pelleted at 13,000xg, and flash frozen in liquid nitrogen for storage after the supernatant was removed. Cell pellets were lysed in double distilled water following three cycles of freeze-thawing in a water bath sonicator. Subsequently, lipids were extracted according to Folch's Method. The organic phase of each sample, normalized by tissue weight, were then separated using ultra high performance liquid chromatography coupled to tandem mass spectrometry (UHPLC-MSMS).[133] UHPLC analysis was performed employing a C30 reverse-phase column (Thermo Acclaim C30, 2.1 x 250 mm, 3 μM, operated at 55° C; Thermo Fisher Scientific) connected to a Dionex UltiMate 3000 UHPLC system and a Q-Exactive Orbitrap high resolution mass spectrometer (Thermo Fisher Scientific) equipped with a heated electrospray ionization (HESI-II) probe. Extracted lipid samples were dissolved in 2:1 methanol:chloroform (v/v) and 5 μl of each sample was analyzed separately using positive and negative ionization modes, respectively. Mobile phase A consisted of 60:40 water/acetonitrile (v/v), 10 mM ammonium formate and 0.1% formic acid, and mobile phase B consisted of 90:10 isopropanol/acetonitrile (v/v), 10 mM ammonium formate and 0.1% formic acid. Lipids were separated over a 90 min gradient; during 0–7 minutes, elution starts with 40% B and increases to 55%; from 7 to 8 min, increases to 65% B; from 8 to 12 min, elution is maintained with 65% B; from 12 to 30 min, increase to 70% B; from 30 to 31 min, increase to 88% B; from 31 to 51 min, increase to 95% B; from 51 to 53 min, increase to 100% B; during 53 to 73 min, 100% B is maintained; from 73 to 73.1 min, solvent B was decreased to 40% and then maintained for another 16.9 min for column re-equilibration. The flow-rate for chromatographic separation was set to 0.2 mL/min. The column oven temperature was set at 55° C, and the temperature of the autosampler tray was set to 4° C. The spray voltage was set to 4.2 kV, and the heated capillary and the HESI were held at 320° C and 300° C, respectively. The S-lens RF level was set to 50, and the sheath and auxiliary gas were set to 35 and 3 units, respectively. These conditions were held constant for both positive and negative ionization mode acquisitions. External mass calibration was performed using the standard calibration mixture every 7 days. MS spectra of lipids were acquired in full-scan/data-dependent MS2 mode. For the full-scan acquisition, the resolution was set to 70,000, the AGC target was 1e6, the maximum injection time was 50 msec, and the scan range was m/z = 133.4–2000. For data-dependent MS2, the top 10 precursor selection in each full scan were isolated with a 1.0 Da window, fragmentation using stepped normalized collision energy of 15, 25, and 35 units, and analyzed at a resolution of 17,500 with an AGC target of 2e5 and a maximum injection time of 100 msec. The underfill ratio was set to 0. The selection of the top 10 precursors was subject to isotopic exclusion with a dynamic exclusion window of 5.0 sec. All data were analyzed using the LipidSearch version 5.0 SP (Thermo Fisher Scientific) and all identified species (grade A, B) were reported.

RNASeq

40,000 MIN6 cells/well were seeded in 96-well plates 24 h prior to treatment in three replicates. FFA library compound plates were transferred into assay plates which were then incubated for 24 h (n=6). RNA was extracted from cells using TCL buffer (#1031576, Qiagen) with 1% beta-mercaptoethanol followed by an RNA clean-up with Agencourt RNA cleanup XP (#A63987, Beckman Coulter). Bulk RNA (1 μl) was added to a 3 step cDNA synthesis reaction with 3'RT (5'- AGCAGTGGTATCAACGCAGAGTAC(T30)VN-3', IDT), template switching (5'-AAGCAGTGGTATCAACGCAGAGTACrGrG+G-3', Qiagen), and ISPCR (5'-AAGCAGTGGTATCAACGCAGAGT-3', IDT) oligos from the SMART-seq2 protocol.[134] cDNA was purified using AMPure XP Agencourt (#100609, Beckman Coulter) and quantified using Qubit dsDNA High Sensitivity (#102689, Life Technologies). Samples were diluted to 0.2 ng/ul in TE and tagmented (Nextera XT DNA Library Preparation Kit (#FC-131-1096, Illumina). Indexing was performed using the Nextera XT Index Kit (#FC-131-1001, Illumina). Final libraries were QCed using the Qubit dsDNA High Sensitivity kit and Bioanalyzer High Sensitivity DNA Kit (#5067-4627, Agilent). Libraries were sequenced at a concentration of 1.8 pM on a NextSeq with a 75 cycle v2 kit (#TG-160-2002, Illumina) with a read structure of Read 1 37bp, Read 2 37bp, Index 1 8bp, and Index 2 8bp. Each sample had approximately 4 million reads.

Cell Painting

MIN6 cells were seeded at a density of 15,000 per well in a 384-well plate (Perkin Elmer, CellCarrier Ultra, #6057300). After 24 h recovery, cells were treated with the FFA library and incubated for 24 h. Cell staining and fixation was performed according to previous protocols.[31] Images were acquired with the Opera Phenix High Content Screening System (#HH14000000, Perkin Elmer) with a 63X/1.15NA water immersion lens. Image quality control was carried out using CellProfiler 2.2.0[115] and CellProfiler Analyst[116] according to a prior machine-learning based protocol.[135] Image illumination correction and analysis were performed in CellProfiler (pipelines available upon request). After analysis, the data were compiled and normalized in Cytominer (code available at https://github.com/cytomining/cytominer) as described previously.[31] Briefly, single cell level features were aggregated per well by computing averages. The mean values and dispersion of the 2202 features measured in all samples were normalized to negative controls (BSA). Features with near-zero variance were removed, and a non-redundant feature set was created by inspecting pairwise correlations. The remaining 1222 features comprise the morphological profile of a given well.

CMIP KO Clone Selection

Lentivirus containing a plasmid programmed to express either *Cmip*-specific sgRNA (ACGTCTTCAATGGCGCTGTAGG, Millipore Sigma, Sanger Clone MM5000005403) or non-targeting control sgRNA (Millipore Sigma, CRISPR20-1EA) was obtained through transfecting HEK293T cells with these plasmids in combination with a second generation CMV lentiviral packaging system and FuGENE transfection agent (E2311, Promega).

MIN6 cells stably expressing Cas9 were infected with this lentivirus at half volume with 8 μg/ml polybrene (TR-1003-G, Sigma) overnight. The media was changed 12 h later, and 48 h after the first media change, 1 μg/ml of puromycin was added to the media. After one week of puromycin selection, the cultures were dispersed into single cells, seeded into 96-well plates for expansion, and sequenced for *Cmip* mutations. One WT clone and one possessing a truncation within the first 15% of the longest CMIP isoform were used for the experiments described.

To derive CMIP KO cells from the human iPSC-beta cell line, we delivered Cas9-RNP complexes with either *CMIP*-specific sgRNA or non-targeting sgRNA (same as Min6 above) to the parental iPSC cells using a Lonza nucleofector kit. Upon confirmation of successful transfection and generation of a stable knockout line, single clones were isolated and sequenced to ultimately identify the clone used in the studies described.

CMIP Overexpression for Rescue Studies

To re-express CMIP back into the MIN6 CMIP KO line, we obtained lentivirus from VectorBuilder containing a mouse *Cmip* ORF (NM_001163262.1) with a modified PAM site under a CMV promoter and accompanied by a neomycin resistance gene. We used the same vector with amino acids 2-83 of E. coli beta-galactosidase as a substitute for the *Cmip* ORF for our control line. 600,000 cells were seeded into each well of a 6-well plate and one week later were infected with up to 100ul virus per well (and 8 ug/ml polybrene (TR-1003-G, Sigma)) overnight. The media was changed 12 h later, and 48 h after the first media change, 800 μg/ml of G418 was added to the media. After selection for one week, the cells were used for the experiments described.

Cell Viability

For the high throughput cell viability assay, cells were seeded in 384-well plates (Perkin Elmer, CellCarrier Ultra, #6057300) and treated for 24, 48 and 72 h with the FFA library (n=7 / FFA). Just before readout, cell nuclei were stained with Hoechst (Thermo Fisher Scientific) for 1 h at 37˚C and imaged with the Opera Phenix High Content Screening System (#HH14000000, Perkin Elmer). Number of counted nuclei was determined with the image analysis software Harmony (PerkinElmer) and used as a proxy for cell viability. For validation experiments, cells were treated for 48 h with representative FFAs in CellCarrier-384 Ultra Microplates. Caspase 3/7 (Thermo Fisher Scientific, #C10423) activation and propidium iodide (Thermo Fisher Scientific, #P3566) staining were used to calculate the fraction of apoptotic cells and dead cells, respectively. Single cells were identified and counted after staining their nuclei with Hoechst. Fluorescence intensities were measured and the threshold for caspase 3/7 and propidium iodide positive staining was determined manually. Cell viability was calculated as the fraction of cells that were neither caspase 3/7 nor propidium iodide positive. For the EA dose-response curve, MIN6 cells were grown as described and then treated for 65 hours with BSA, EA or OA. The concentrations were (in mM): 0.7, 2.1, 6.2, 18.5, 55.6, 166.7, 500, 1000 and were prepared by serial dilution from a stock concentration. Cell viability was assessed as described.

iPSC-derived microglia

On day 30 of the differentiation, iMGLs were plated in 96-well plates (Perkin Elmer, CellCarrier) at a density of 20,000 cells per well. One day before treatment, FFA and BSA were reconstituted in iMGL media and gently rocked overnight at room temperature. At day 40, iMGL were treated with a final concentration 250 μM of each FFA or BSA for 24 h followed by live imaging. Cells were imaged using the Opera Phenix confocal system using a 20X objective, temperature was maintained at 37 °C and CO2 at 5% during the imaging period. One plane was taken per picture and 20 images were taken per well. Harmony software was used for analysis, flatfield correction (Basic Method) and cell identification using EGFP signal (common Threshold 0.02; area >50 μm^2). Total number of cells per well was used for quantification with an n=4 for all conditions.

Kidney tubular epithelial cells

Prior to treatment, BSA-bound FFAs were reconstituted and incubated overnight in RenaLife media at room temperature. Cells were seeded in CellCarrier-384 Ultra Microplates and maintained at 37°C with 5% CO2. Cells were treated with 500 μM FFA or BSA for 15 h

followed by live imaging using the Opera Phenix High Content Screening System. Number of cells and number of dead cells was determined on Harmony image analysis software using digital phase contrast and propidium iodide staining (Thermo Fisher Scientific, #P3566), respectively. Viability was assessed by calculating the number of propidium iodide-negative cells per total number of cells per well (n=4).

Western Blot

MIN6 cells were lysed (#9803, Cell Signaling Technology) in the presence of protease inhibitors (#05892791001, Roche) and phosphatase inhibitors (#04906837001, Roche). Protein concentrations were quantified with the Pierce BCA Protein Assay Kit (#23225, Thermo Fisher Scientific). NuPAGE LDS sample buffer (#NP0008, Thermo Fisher Scientific) was added to normalized protein lysates together with NuPAGE reducing agent (#NP0004, Thermo Fisher Scientific). Lysates were heated to 95 °C for 5 min prior to SDS-PAGE gel electrophoresis (NuPAGE MES SDS running buffer, Thermo Fisher Scientific, #NP0002). Proteins were transferred to a nitrocellulose membrane (#1704158, BioRad) with the Trans-Blot Turbo TM Blotting System (#1704155, BioRad) according to the manufacturer's protocol. Membranes were blocked in 5% Nonfat Dry Milk (#9999S, Cell Signaling Technology) in PBS with 0.1% Tween 20 (PBS-T). AKT and pAKT blots were blocked instead in 5% Bovine Serum Albumin (#1900-0016, LGC Clinical Diagnostics) in PBS-T. Primary antibodies were incubated at 4 °C overnight, secondary antibodies were incubated at room temperature for 1 h. Super Signal West Femto (#34094, Thermo Fisher Scientific) or SuperSignal West Pico (#34087, Thermo Fisher Scientific) were used to visualize immunoreactive bands imaged by G:BOX Chemi XT4 (BOX-CHEMI-XT4, Syngene). Primary antibodies used in this study were CPT1A: (#ab128568, Abcam), ATF4: (#11815, Cell Signaling Technology), CHOP: (#2895, Cell Signaling Technology), CMIP: (NBP2-58180, Novus Bio), AKT: (#9272, Cell Signaling Technology), pAKT: (#4060, Cell Signaling Technology), AMPKα: (#2532, Cell Signaling Technology), pAMPKα: (#2535, Cell Signaling Technology), FOXO1: (#2880, Cell Signaling Technology), pFOXO1: (#9464, Cell Signaling Technology), GAPDH-HRP: (#3683, Cell Signaling Technology). Secondary antibodies used were: anti-rabbit IgG-HRP (#7074, Cell Signaling Technology), anti-mouse IgG-HRP (#7076, Cell Signaling Technology).

Coimmunoprecipitation (co-IP)

Two 10cm dishes of Min6 cells were lysed with 1ml of co-IP lysis buffer (100mM NaCl, 5mM EDTA, 50mM Tris-HCl pH 7.5, 1% NP-40, protease inhibitor tablet, phosphatase inhibitor tablet) after being washed once with ice cold PBS. The lysate was rotated at 4°C for 30m, spun at 13,000xg for 20m at 4°C, and the supernatant was collected. 1mg of protein was combined with 10ug of either CMIP antibody (12851-1-AP, Proteintech) or rabbit IgG control antibody (10500C, Thermo Fisher) and rotated overnight at 4°C. The following day, Pierce Protein A/G Magnetic Beads (88802, Thermo Fisher) were warmed to room temperature, washed twice with 1ml TBS-T (150mM NaCl, 50mM Tris-HCl pH 7.5, 0.05% Tween-20) on a magnet, and resuspended in the original volume of co-IP lysis buffer. 25ul of beads were added to each lysate tube and the solution was rotated at 4°C for 1h. The beads were then washed 3x with 1ml TBS-T, once with 1ml distilled water, and eluted with 30ul of 2X NuPAGE LDS Sample Buffer and 1X NuPAGE Sample Reducing Agent (DTT). The beads were incubated at room temperature for 10m with occasional flicking of the tube, and then the supernatant was extracted on the magnet. The supernatant was incubated at 95°C for 10m and then the samples were run on a gel as detailed in the Western Blot section above. The primary antibodies used for staining were CMIP: (12851-1-AP, Proteintech) and PI3K p85α: (#4292, Cell Signaling Technology).

Immunofluorescence (IF) staining

MIN6 NFkB Immunofluorescence

MIN6 cells grown on 384-well CellCarrier Ultra microplates (#6057308, PerkinElmer) were fixed for 10 min in PBS containing 4% PFA (Electron Microscopy Sciences), permeabilized for 15 min in 0.5% Triton X-100 (Sigma-Aldrich), blocked for 1 h in blocking reagent (100 mM Tris HCL pH 8; 150 mM NaCL; 5 g/L Blocking Reagent (#11096176001, Roche)) and treated for 1.5 h with primary antibody diluted in blocking reagent (NF-κB p65/RELA, Rabbit monoclonal antibody, 1:200, #8242, Cell Signaling Technology). Cells were washed three times in PBS and incubated for 0.5 h with fluorescent-labeled secondary antibody in blocking solution (1:500, Alexa Fluor 568 Goat anti-Rabbit IgG, (#A11036, Thermo Fisher Scientific)). Cytoplasmic actin filaments were stained with Phalloidin conjugated with Alexa 647 (1:40, #A22287, Thermo Fisher Scientific) and nuclei were counterstained with Hoechst (1:2000, #H3570, Thermo Fisher Scientific). Cells were washed three times in PBS and imaged using the Opera Phenix High Content Screening System (#HH14000000, Perkin Elmer). A minimum of nine fields were acquired per well using 20x water immersion objectives in confocal mode. Image analysis was performed using the Harmony software (PerkinElmer). Cell nuclei were first identified using Hoechst staining and a nuclear region was defined for each cell. Phalloidin staining was then used to detect and define the cytoplasmic region of the cell. RELA fluorescent intensity was measured separately in the nuclear and cytoplasmic regions and a threshold for a nuclear translocation was defined using negative (BSA) and positive (TNF) controls. For each well, the fraction of cells identified for RELA nuclear translocation was calculated.

MIN6 LC3B Immunofluorescence

MIN6 cells grown on 384-well CellCarrier Ultra microplates (#6057308, PerkinElmer) were treated for 48 h with 500 μM FFAs or 25 nM of rapamycin (Sigma-Aldrich, R8781) or bafilomycin A1 (Sigma-Aldrich SML1661). Cells were fixed for 20 min in ice-cold methanol (Sigma-Aldrich, 154903), washed twice with PBS, permeabilized for 15 min in 0.5% Triton X-100 (Sigma-Aldrich, 10789704001), washed twice with PBS, blocked for 1 h in 5% BSA in PBS (LGC Clinical Diagnostics, 1900-0016) and incubated for 1.5 h with primary antibody diluted in blocking reagent (Lc3b (D11) XP Rabbit mAb, 1:500, #3868, Cell Signaling Technology). Cells were washed four

times in PBS and incubated for 45 min with fluorescent-labeled secondary antibody in blocking solution (1:500, Alexa Fluor 568 Donkey anti-Rabbit IgG, (#A10042, Thermo Fisher Scientific)). Nuclei were counterstained with Hoechst (1:2000, #H3570, Thermo Fisher Scientific). Cells were washed four times in PBS and imaged using the Opera Phenix High Content Screening System (#HH14000000, Perkin Elmer). A minimum of nine fields were acquired per well using 63x water immersion objectives in confocal mode. Image analysis was performed using the Harmony software (PerkinElmer). Cell nuclei were first identified using Hoechst staining and a nuclear region was defined for each cell. LC3B puncta were then detected based on intensity and size with rapamycin and bafilomycin treatments serving as controls.

Primary Human Islet Immunofluorescence

Primary human islets were treated two days after dissociation and plating with FFAs at 250 μM, 500 μM, and 1 mM. After treatment for 5 days, the islets were fixed for 20 min in 3% PFA followed by permeabilization for 20 min with 0.2% TritonX-100. Blocking with 2% BSA in PBS (SeraCare, AP-45100-80) was conducted for 1 h at room temperature, followed by primary incubation with c-peptide antibody (Developmental Studies Hybridoma Bank at the University of Iowa, GN-ID4) at 1:100 overnight at 4 °C. The plate was washed 3x with PBS followed by secondary incubation with 568 goat anti-rat (Life technologies, A11077) at 1:1000 and Hoechst (1:2000, #H3570, Thermo Fisher Scientific) for 1 h at room temperature. The plate was then washed 5x with PBS and imaged on the Opera Phenix High Content Screening System (#HH14000000, Perkin Elmer). A minimum of nine fields were acquired per well using a 20x water immersion objective in confocal mode. Image analysis was performed using the Harmony software (PerkinElmer). Beta cells were identified and counted by c-peptide positive staining. All three donors displayed similar trends in c2 toxicity; the data presented in Figure 5C are representative of all donors.

iPSC-Derived Beta Cell Immunofluorescence

IPSC-derived beta cells after 28 days of differentiation as per the protocol listed above were dissociated and seeded at 10,000/well into 96-well Cell Carrier Ultra microplates (Perkin Elmer, CellCarrier Ultra, #6055308) coated with HTB-9-derived ECM. These cells were treated three days later with FFAs at 250 μM, 500 μM, and 750 μM for 24, 48, and 72 h followed by fixation with 4% PFA for 30 min at room temperature. The plates were washed twice with PBS, permeabilized for 15 min with 0.5% Triton-X 100, washed twice again with PBS, and blocked with 5% BSA in PBS for 1 h at room temperature. This was followed by primary incubation with c-peptide antibody (Developmental Studies Hybridoma Bank at the University of Iowa, GN-ID4) at 1:100 overnight at 4 °C. The plate was washed 3x with PBS followed by secondary incubation with 568 goat anti-rat (Life technologies, A11077) at 1:1000 and Hoechst (1:2000, #H3570, Thermo Fisher Scientific) for 1 h at room temperature. The plate was then washed thrice with PBS and imaged on the Opera Phenix High Content Screening System (#HH14000000, Perkin Elmer). A minimum of nine fields were acquired per well using a 20x water immersion objective in confocal mode. Image analysis was performed using the Harmony software (PerkinElmer) and the cells were counted.

ER Calcium Levels

MIN6 cells were plated in 384-well plates (Aurora, Black 384 SQ Well 188 micron Film, #1022-10110) and treated with the FFA library for 24 h prior to readout (n=5 / FFA). Cells were carefully washed three times with HBSS (with calcium, Thermo Fisher Scientific, #14025076) using an automated simultaneous pipettor (analytikjena CyBio Well vario) and incubated with the fluorescent calcium indicator Fluo4 (2 μM, Life Technologies, #F14202) in DMEM without supplementation for 1 h at room temperature. Then, cells were washed again in HBSS (with calcium) and incubated for another 30 min at room temperature in DMEM without supplementation. Just before the readout, cells were washed in calcium free assay buffer solution (140 mM NaCl, 5 mM KCl, 10 mM HEPES, 2 mM $MgCl_2$, 10 mM EGTA, 10 mM Glucose) and left with 25 μl assay volume per well. Assay plates were immediately transferred to the FLIPR Tetra High-Throughput Cellular Screening System. The plate was recorded with a frequency of 1Hz for 10 min. Baseline was recorded for 30 s before the automated liquid transfer system of the FLIPR added the SERCA inhibitor Thapsigargin (final concentration 10 μM) in calcium free assay buffer. The resulting passive efflux of calcium from the ER induced a transient cytosolic fluorescence signal and the peak amplitudes were used to indirectly quantify ER calcium levels (see Figure S3A). The resulting trajectories were corrected for a pipetting artifact and baseline normalized. Log_2 Fold changes were calculated according to plate location specific negative (BSA) controls. We allowed for the exclusion of one outlier / FFA / plate (n=5) based on a 3-sigma cutoff. P-values were calculated with Student's t-test (two-sided) and corrected for multiple testing (Benjamini & Hochberg).

Glucose Stimulated Insulin Secretion (GSIS)

To measure GSIS, cells were plated in 96-well plates (Perkin Elmer, CellCarrier Ultra, #6055308) and treated with the FFA library for 24 h prior to readout (n=6 / FFA). First, cells were pre-incubated in Krebs Ringer Buffer (KRB) with 2.8 mM glucose for 1 h and then stimulated with fresh KRB containing 16.7 mM glucose for another hour. The supernatant was then transferred to a mouse insulin ELISA (Thermo Fisher, EMINS) at a dilution of 1:150. The cells were imaged on the Opera Phenix High Content Screening System, (#HH14000000, Perkin Elmer) and subsequently counted via Hoechst nuclear staining using Harmony software (PerkinElmer). A minimum of four fields were acquired per well using a 10x air objective in a confocal mode. The insulin concentrations measured via ELISA were normalized to the number of cells in each respective well.

Membrane Fluidity Assay

This assay has been well established and optimized in INS-1E cells, a rat beta cell line. INS-1E cells were seeded at 20,000 cells per well in a CellCarrier Ultra 96-well plate (Perkin Elmer). Cells were incubated for 24 h, washed once with PBS, treated with BSA-bound

fatty acids in a serum-free media and further incubated for 18 h at 37°C. Cells were washed twice with PBS and stained with Laurdan dye (6-dodecanoyl-2-dimethylaminoaphthalene) (Thermofisher) at 10 μM for 45 min. Cells were washed twice with PBS and images were acquired using an Opera Phenix High-Content Screening system (Perkin Elmer). Temperature (37°C) and carbon dioxide (5%) were controlled during live-cell imaging. Cells were excited with a 405 nm laser and the emission recorded between 435 and 480 nm (ordered phase) and between 500 and 550 nm (disordered phase). Images were analyzed using Harmony High-Content Imaging and Analysis Software (Perkin Elmer) and data represented as general polarization (GP) index as calculated by GP = ($intensity_{order}$ - $intensity_{disorder}$)/($intensity_{order}$ + $intensity_{disorder}$).[136,137]

QUANTIFICATION AND STATISTICAL ANALYSIS

Unless otherwise stated all computational and statistical analysis in this study has been performed in Python and R. Statistical details for each experiment can be found in the figure legends.

Lipidomics

A blocked experimental design with one replicate of each FFA in the library, together with multiple BSA controls per 96-well plate, was chosen (n=3). Raw lipidomic profiles received from the Metabolomics Platform at the Broad Institute were filtered for samples with strongly deviating sample medians (manual cutoff, 7 out of 280 or 3% of the samples were discarded). Lipid metabolites with more than 30% of missing data points were removed, otherwise missing values were substituted with 50% of the minimum value of the respective metabolite's intensity. To account for variations in total amount of captured metabolites, samples were scaled towards the global sample median. Only annotated lipid metabolites were used for further differential abundance analysis. We sought to understand the relationship between structural features of externally added FFAs and changes in the triglyceride fraction of the cells (Figure 1C). For each externally added FFA, triglyceride intensity deviations from the BSA control were summed based on the structural feature of interest (number of C-atoms, number of double bonds). Then, triglyceride profiles of externally added FFAs were summarized based on the structural feature of interest of the FFAs (number of C-atoms, number of double bonds) and normalized to the number of FFAs making up each group. For assessment of the global lipidome in response to erucic and palmitic acid, lipid metabolites were filtered as described and subsequently imported into lipidR.[121] Differential analysis of lipid abundance was calculated using the empirical Bayes procedure. Fold change in lipid abundance (EA vs. PA) was then normalized based on noted structural features (number of C-atoms, number of double bonds) and visualized in R. Network analysis of the biochemical relationship between differentially abundant lipid species was performed using the Lipid Network Explorer with default settings.[117]

RNASeq pipeline

A blocked experimental design with one replicate of each FFA in the library together with multiple BSA controls per 96-well plate was chosen (n=6). Raw data from NextSeq runs were de-multiplexed and converted to sample specific fastq files. Alignment was performed with STAR,[118] reads were counted with HTSeq[127] and QC metrics were generated with RNA-SeQC.[119] The resulting count matrix was filtered by column for samples with more than 10^3 detected genes (counts > 0) and by row for coding genes (as defined by the MGI database) with a row sum across all samples > 500 counts (with a total number of 500 samples). The resulting normalized and filtered count matrix was then variance stabilized using the vst method from the DESeq2 R package.[122] Surrogate variable analysis (SVA, R package)[123] was performed on the vst count matrix to account for linear batch effects. In addition, we performed differential expression analysis with DESeq2 for each sample, including derived surrogate variables to the linear model. To cluster the samples, we chose the top 500 most common significant differentially expressed genes ($p_{adj} < 0.05$) across the entire dataset. Samples were either transformed to z-scores or replicates were collapsed by calculating their signal to noise ratio (with respect to the BSA control) before performing hierarchical clustering based on Euclidean distance and Ward's linkage method. Clusters were extracted with the Dynamic Tree Cut function.[124] After assigning each FFA to a cluster, we performed differential expression analysis based on cluster labels and BSA controls (based on the vst count matrix) and calculated adjusted p-values for each gene (Mann–Whitney U, Bonferroni).

Gene Set Enrichment Analysis

For gene set enrichment analysis (GSEA), gene lists for each FFA transcriptome were ranked by log_2 fold changes as compared to BSA control to weigh genes according to their differential expression vs control. MsigDB H: HALLMARK gene sets, C2: KEGG and REACTOME gene sets and C5: GO BP gene sets were tested for enrichment.[20,120] 250 Genesets with the most common, significant differential enrichment across the whole FFA library were selected and transformed into a normalized enrichment score (NES) matrix. Hierarchical clustering of those genesets resulted in the gene modules presented in Figure 2A. Pearson correlation analysis of human islet gene expression[91] was performed using MATLAB 2020a (MathWorks), as previously described.[138] Genes significantly correlated with *CMIP* (FDR < 0.01,Benjamini-Hochberg) were subjected to KEGG pathway analysis using Metascape and visualized using Cytoscape.

Rank-rank hypergeometric overlap (RRHO)

The R package RRHO2[125] was used to perform RRHO analysis to evaluate the cutoff-free overlap in differential expression results from FFA Clusters (C1-C5) versus human islets[28] and mouse pancreatic beta cells.[43] RRHO2 plots show a heatmap with four

quadrants to display the overlap between expression list comparisons. This includes: downregulated observations in both data sets (top right, Figures S2E and S2F), downregulated in the comparative data and upregulated observations in our data (bottom right, Figures S2E and S2F), upregulated in the comparative data and downregulated observations in our data (top left, Figures S2E and S2F) and upregulated observations in both data sets (bottom left, Figures S2E and S2F). For each comparison, one-sided enrichment tests were used on -log(p-values) with default step size for each quadrant.

Structural analysis of FFAs

Molecular structural features were generated with the MOE software. A complete list of generated features are summarized in Table S5. Detailed descriptions of these features are available in the MOE user manual (v2016.08). The molecular feature matrix was filtered for non-constant features across the FFA library and transformed into z-scores. To decrease the linear dependence between features, meta-features were extracted from the original molecular features by hierarchical clustering based on Pearson correlation and Ward's linkage method (cutreeDynamic, WGCNA, R package).[124] Clustering was performed iteratively until the maximum Pearson r correlation coefficient between any two meta-features was less than 0.8 (n=3 iterations). The first principal component of molecular feature clusters were used to define meta-features.

The random forest classifier (RFC) was performed (randomForest; R package).[126] Optimal values for ntree (number of trees to grow) and mtry (number of variables randomly sampled as candidates at each split) were determined empirically based on the classification accuracy of the RFC run on the entire dataset. The RFC was then run with leave-one-out cross validation. Meta-feature importance measures for RFC prediction were calculated (importance).

Morphological feature analysis

Confocal images were acquired as described for Cell Painting using the Opera Phenix High Content Screening System (#HH14000000, Perkin Elmer).[31] Image analysis was performed using Harmony software (PerkinElmer). Single nuclei were first identified using Hoechst staining. Associated cell bodies around each nuclei were identified by the ''find cytoplasm function'' method A (individual cutoff 0.1) from the Harmony software in the 488 nm channel. ER and mitochondrial regions were identified (Find Image Region) based on their respective channels (stained with Concanavalin A and MitoTracker respectively) For each cell, the standard morphological features (area and roundness); as well as advanced STAR (Symmetry, Threshold compactness, Axial or Radial) and SER (Spots, Edges, Ridges) morphology for ER and mitochondria were calculated. A full list of extracted features is summarized in Table S6. Data was exported per cell object, and downstream analysis was performed in R.

MAGMA analysis pipeline

The MAGMA software[22] (v 1.07) was used to perform SNP annotation, gene analysis to generate ranked lists of genes from GWAS summary statistics and gene set analysis (GSA) according to the instructions provided in the user manual. For multiple hypothesis testing we used a permutation-based approach to generate an empirical Null Hypothesis to account for the enrichment of beta cell genes in previous T2D GWAS analyses. For each gene set, we generated 1000 randomly sampled gene sets based on the MIN6 transcriptome of the same size and calculated the FDR accordingly.

Cell Metabolism, Volume *35*

Supplemental information

FALCON systematically interrogates free fatty acid biology and identifies a novel mediator of lipotoxicity

Nicolas Wieder, Juliana Coraor Fried, Choah Kim, Eriene-Heidi Sidhom, Matthew R. Brown, Jamie L. Marshall, Carlos Arevalo, Moran Dvela-Levitt, Maria Kost-Alimova, Jonas Sieber, Katlyn R. Gabriel, Julian Pacheco, Clary Clish, Hamdah Shafqat Abbasi, Shantanu Singh, Justine C. Rutter, Martine Therrien, Haejin Yoon, Zon Weng Lai, Aaron Baublis, Renuka Subramanian, Ranjan Devkota, Jonnell Small, Vedagopuram Sreekanth, Myeonghoon Han, Donghyun Lim, Anne E. Carpenter, Jason Flannick, Hilary Finucane, Marcia C. Haigis, Melina Claussnitzer, Eric Sheu, Beth Stevens, Bridget K. Wagner, Amit Choudhary, Jillian L. Shaw, Juan Lorenzo Pablo, and Anna Greka

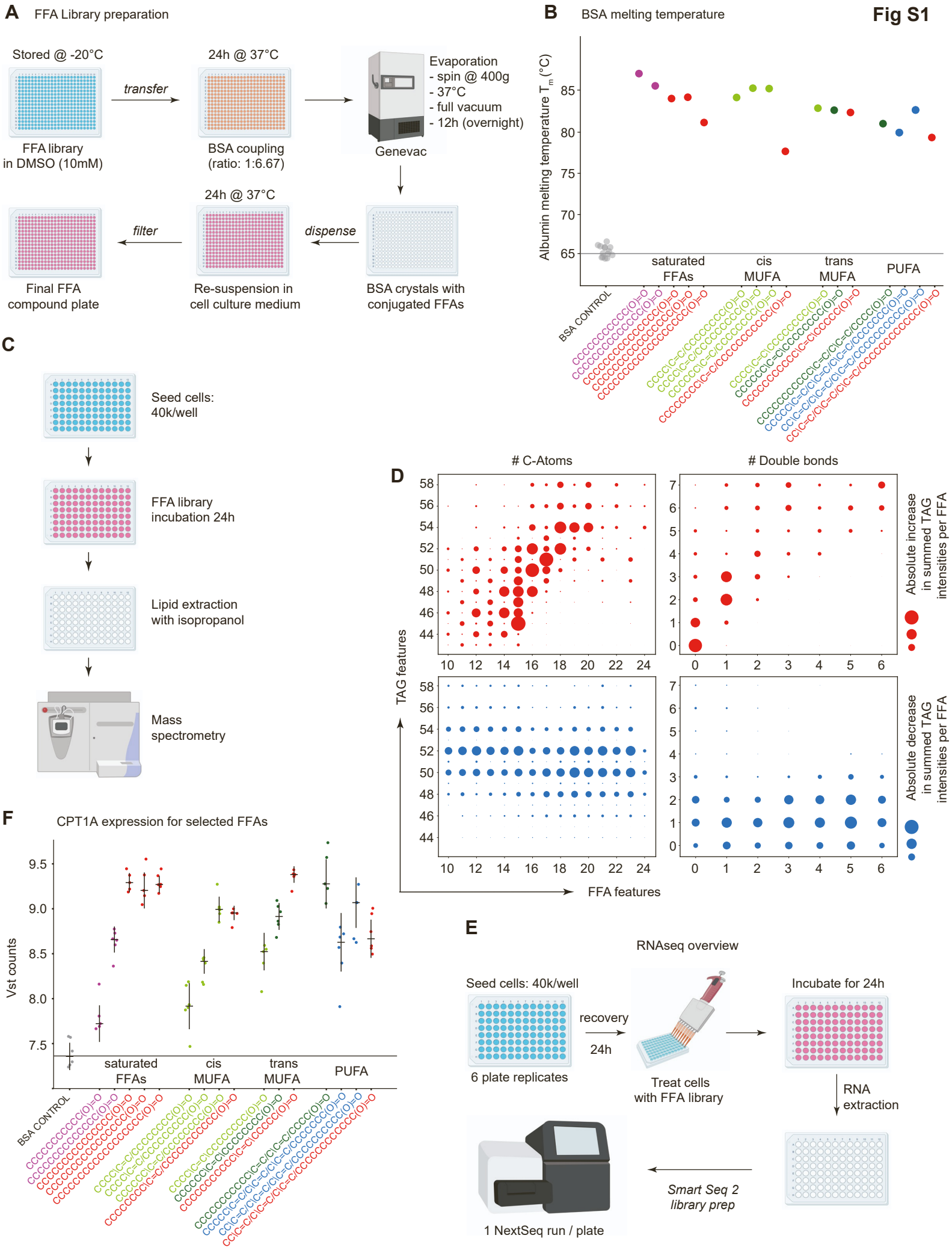
A
FFA Library preparation
Stored @ -20°C
FFA library
in DMSO (10mM)
transfer
24h @ 37°C
BSA coupling
(ratio: 1:6.67)
Evaporation
- spin @ 400g
- 37°C
- full vacuum
- 12h (overnight)
Genevac
dispense
BSA crystals with
conjugated FFAs
24h @ 37°C
Re-suspension in
cell culture medium
filter
Final FFA
compound plate
B
BSA melting temperature
Albumin melting temperature Tm (°C)
saturated FFAs
cis MUFA
trans MUFA
PUFA
BSA CONTROL
C
Seed cells:
40k/well
FFA library
incubation 24h
Lipid extraction
with isopropanol
Mass
spectrometry
D
C-Atoms
Double bonds
TAG features
FFA features
Absolute increase
in summed TAG
intensities per FFA
Absolute decrease
in summed TAG
intensities per FFA
E
RNAseq overview
Seed cells: 40k/well
6 plate replicates
recovery
24h
Treat cells
with FFA library
Incubate for 24h
RNA
extraction
Smart Seq 2
library prep
1 NextSeq run / plate
F
CPT1A expression for selected FFAs
Vst counts
saturated FFAs
cis MUFA
trans MUFA
PUFA
BSA CONTROL

Fig. S1. Design and validation of FALCON, related to Figure 1. (A) Protocol overview describing major steps of the procedure for preparing FFAs. (B) Shift in bovine serum albumin (BSA) melting temperature Tm (y-axis). After library preparation, structurally representative FFAs (structure SMILES, x-axis) consistently increased Tm confirming successful BSA:FFA loading. Colors represent cluster identities (Fig. 1D). (C) Overview of sample preparation for lipidomics experiment. (D) Lipidomic analysis indicated that cells exposed to the library of 61 externally applied FFAs incorporated them into their TAG fraction as detected by mass spectrometry. Qualitative correlation of structural features (number of C atoms, number of double bonds) of externally applied FFAs (x-axis) versus structural features of triglycerides (TAGs, y-axis) detected by lipidomics (Methods). Upper two panels (red dots) show absolute increases in summed triglyceride intensities per FFA, lower two panels (blue dots) show absolute decreases in summed triglyceride intensities per FFA (negative control). (E) RNAseq protocol overview. (F) *Cpt1a* expression for selected FFAs. Consistently significant differential expression (padj < 0.05) confirmed successful delivery of FFAs to the cells.

Fig S2

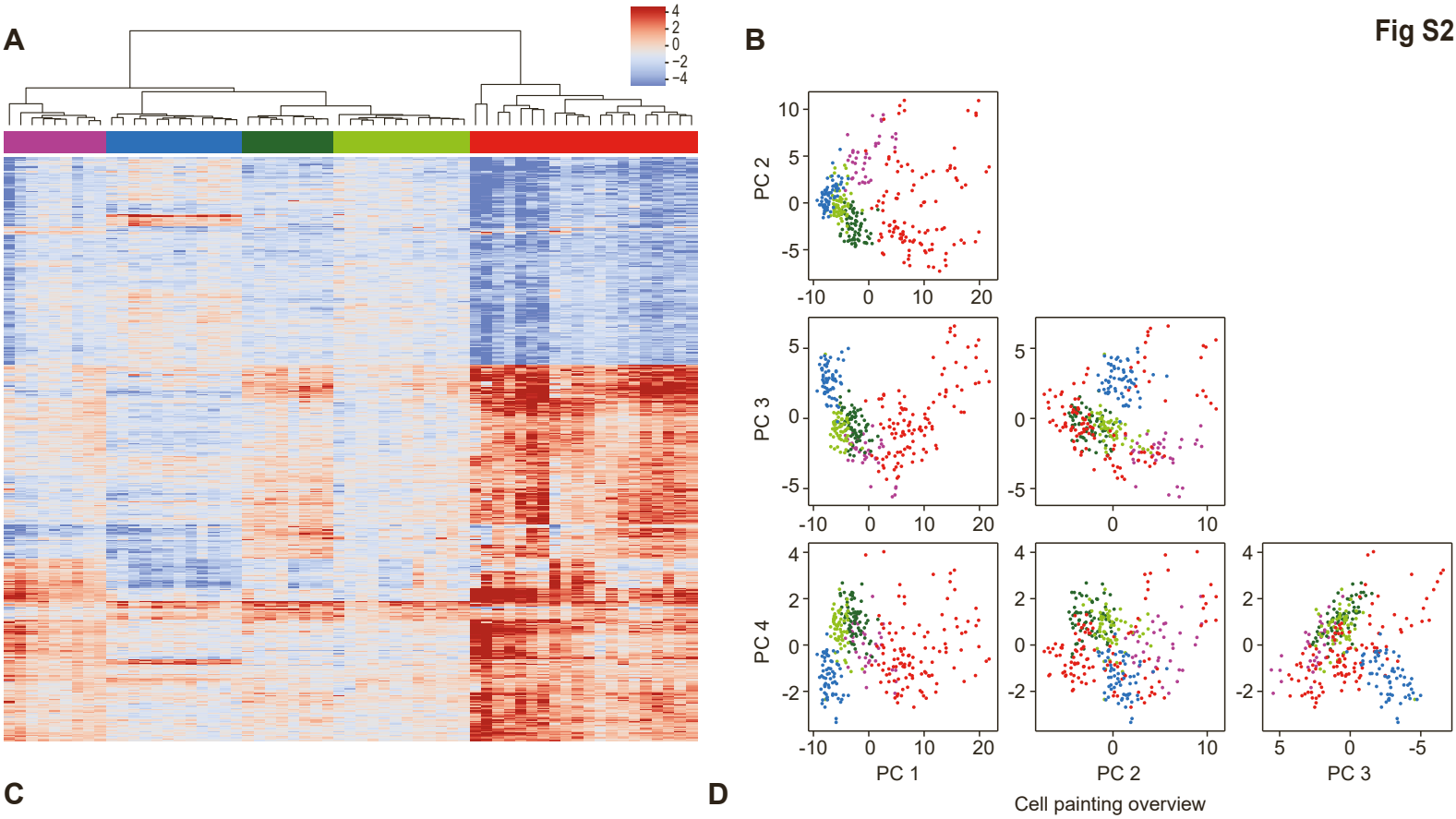
A
B
PC 1
PC 2
PC 3
PC 4
Cell painting overview

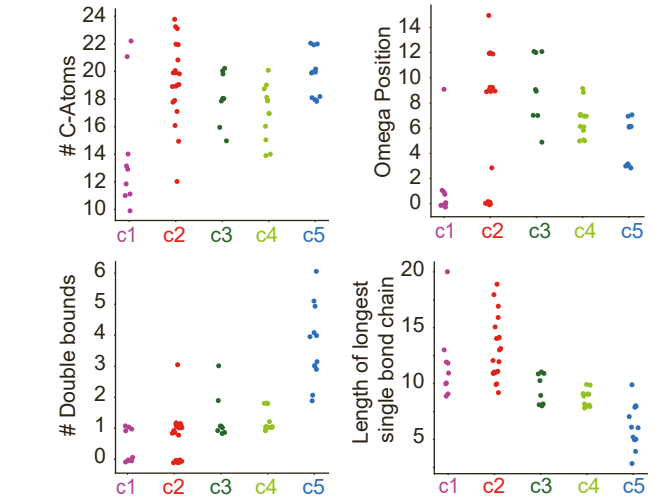
C
C-Atoms
Omega Position
Double bounds
Length of longest single bond chain
c1
c2
c3
c4
c5

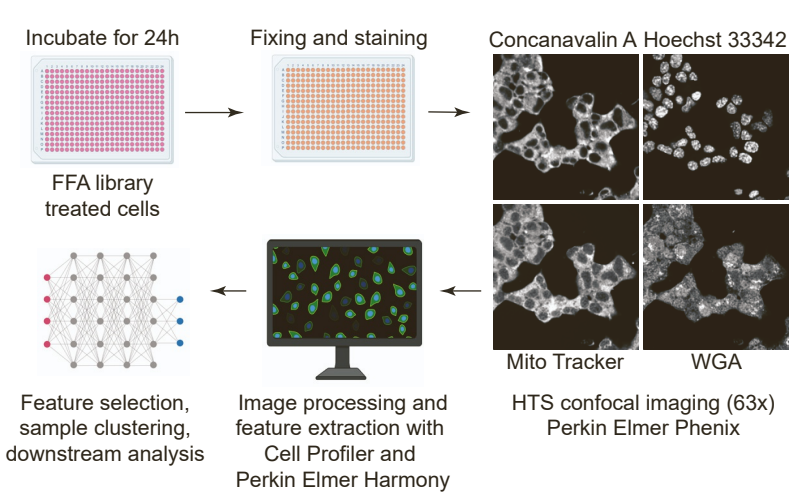
D
Incubate for 24h
Fixing and staining
Concanavalin A
Hoechst 33342
FFA library treated cells
Mito Tracker
WGA
Feature selection, sample clustering, downstream analysis
Image processing and feature extraction with Cell Profiler and Perkin Elmer Harmony
HTS confocal imaging (63x) Perkin Elmer Phenix

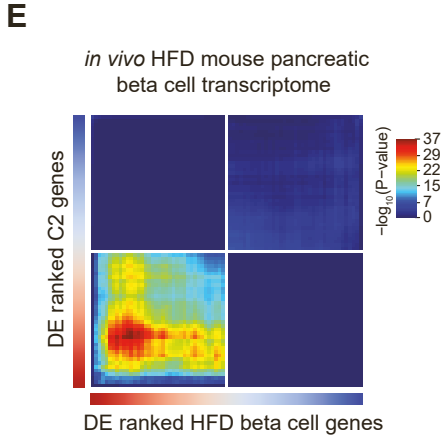
E
in vivo HFD mouse pancreatic beta cell transcriptome
DE ranked C2 genes
DE ranked HFD beta cell genes
−log10(P−value)

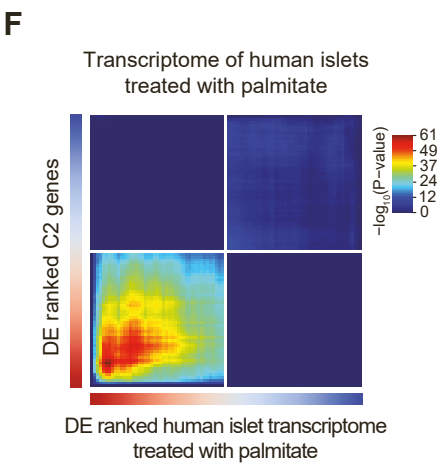
F
Transcriptome of human islets treated with palmitate
DE ranked C2 genes
DE ranked human islet transcriptome treated with palmitate
−log10(P−value)

Fig. S2. Cross-validation of RNAseq-derived clusters with Cell Painting and existing lipotoxicity datasets, related to Figure 1. (A) Hierarchically clustered heatmap based on z-scores of top 500 differentially expressed genes across the entire dataset (collapsed replicates). Clusters were extracted with the Dynamic Tree Cut function[154]. (B) Corner plot of first four Principal Components (PC) of all replicates, capturing 75% of the total variance in the dataset. Colors represent FFA cluster identities (as in Fig. 1D). (C) The structural characteristics of each FFA including number of carbon atoms, number of double bonds, omega position (distance from omega carbon to first double bond), and length of the longest single bond chain are mapped across each cluster. Cluster number and color corresponding to that seen in Fig. 1D are along the x-axis; structural characteristic distribution of FFAs within each cluster is found along the y-axis. (D) Overview of the Cell Painting method. (E,F) Rank-rank hypergeometric overlap (RRHO) maps show significant overlap of the c2-derived lipotoxicity signature with published transcriptomes of pancreatic beta cells isolated from mice fed a high fat diet (E) and human islets exposed to palmitate (F).

A Calcium Imaging Assay with the Molecular Devices FLIPR

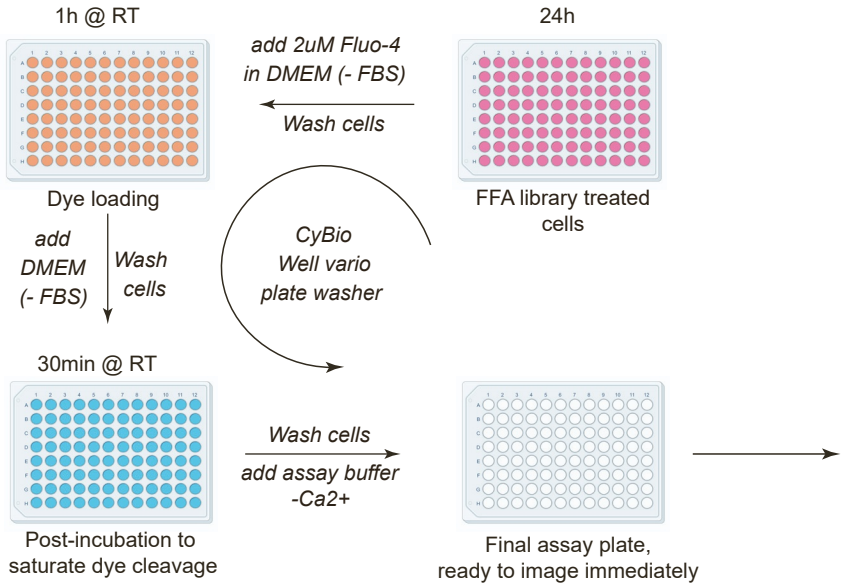

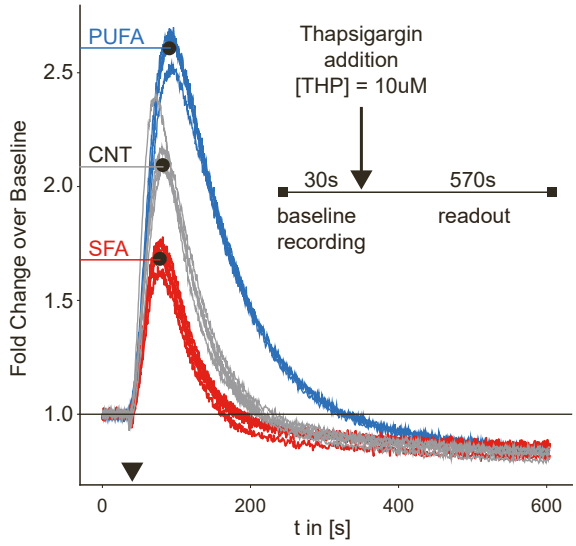

B

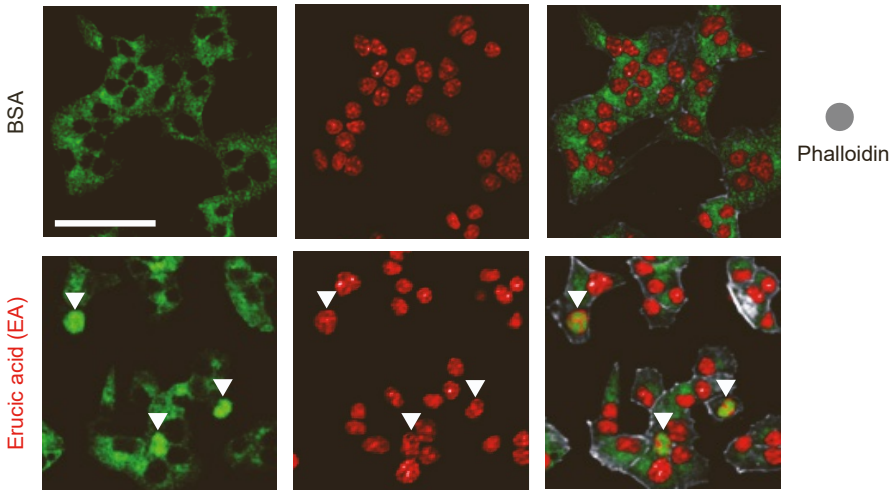

C

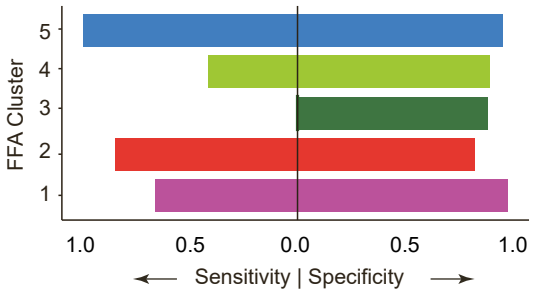

D

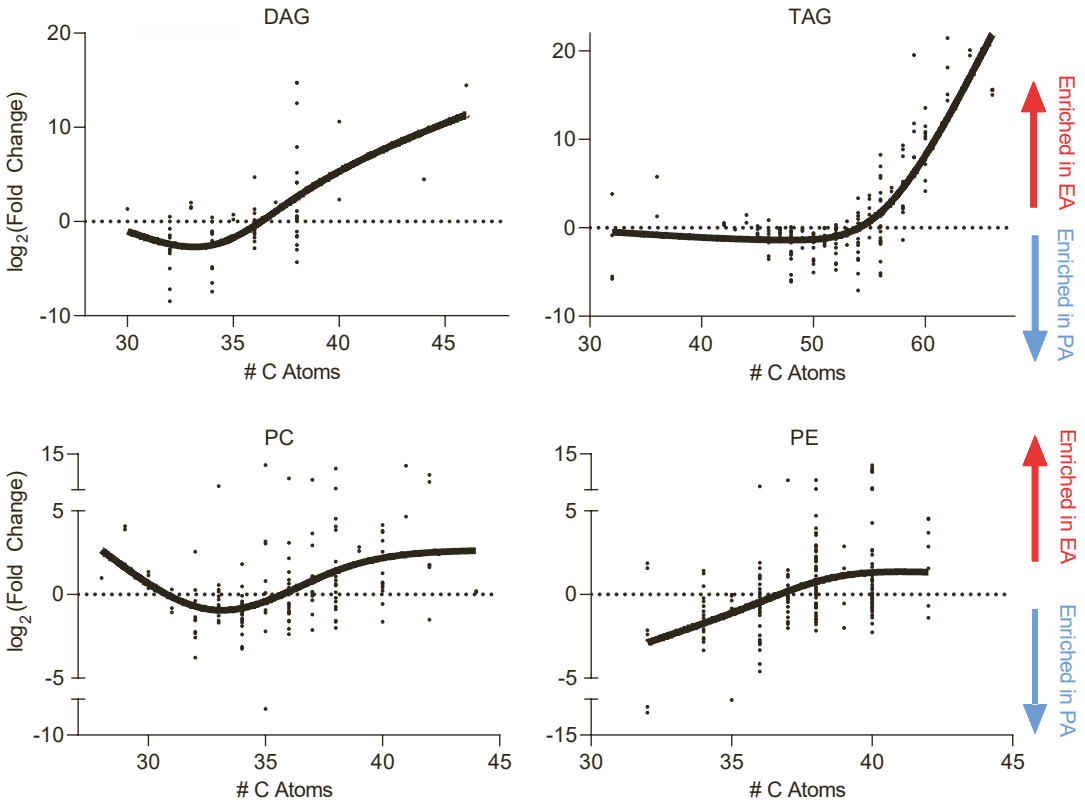

E

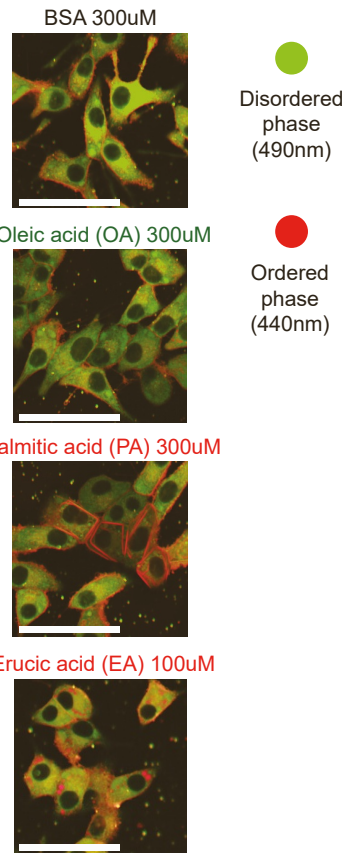

Fig S3. Toxic FFAs alter ER calcium, NFkB signaling, the cellular lipidome, and membrane fluidity, related to Figures 2, 4-5. (A) Overview of the Ca2+ imaging protocol used to quantify dynamic changes in cytosolic Ca2+ levels. Right: Representative example trajectories (n = 5 replicates) of thapsigargin-stimulated (10 mM, black arrow) Ca2+ signals, as fold changes over baseline (y-axis). The inset outlines the measurement protocol. (B) Representative images from immunofluorescence of nuclear translocation of RELA (green) upon exposure to EA (t = 18 h). BSA, negative control. Nuclei were stained with Hoechst (red) and the cytoplasmic cytoskeleton with phalloidin (grey). Complete translocation of RELA into the nucleus (white arrows) was detected in EA-treated cells, highlighted in the merged image. Scale bars: 100 μm. (C) Decision tree prediction accuracy (sensitivity and specificity) of assigning FFAs into transcriptomically defined clusters based on a structural meta-feature matrix (see Methods). (D) Log-fold changes in the abundance of specific lipid species between PA-treated and EA-treated samples. Species above the x-axis are enriched in EA-treated samples, and species below are enriched in PA-treated samples. DAG, diglycerides; TAG, triglycerides; PC, phosphatidylcholines; PE, phosphatidylethanolamines. (E) Representative images of INS1E beta cells assayed in Figure 5C highlighting the disordered phase (green) and the ordered phase (red) of the Laurdan dye. Scale bars: 50 μm.

Fig S4

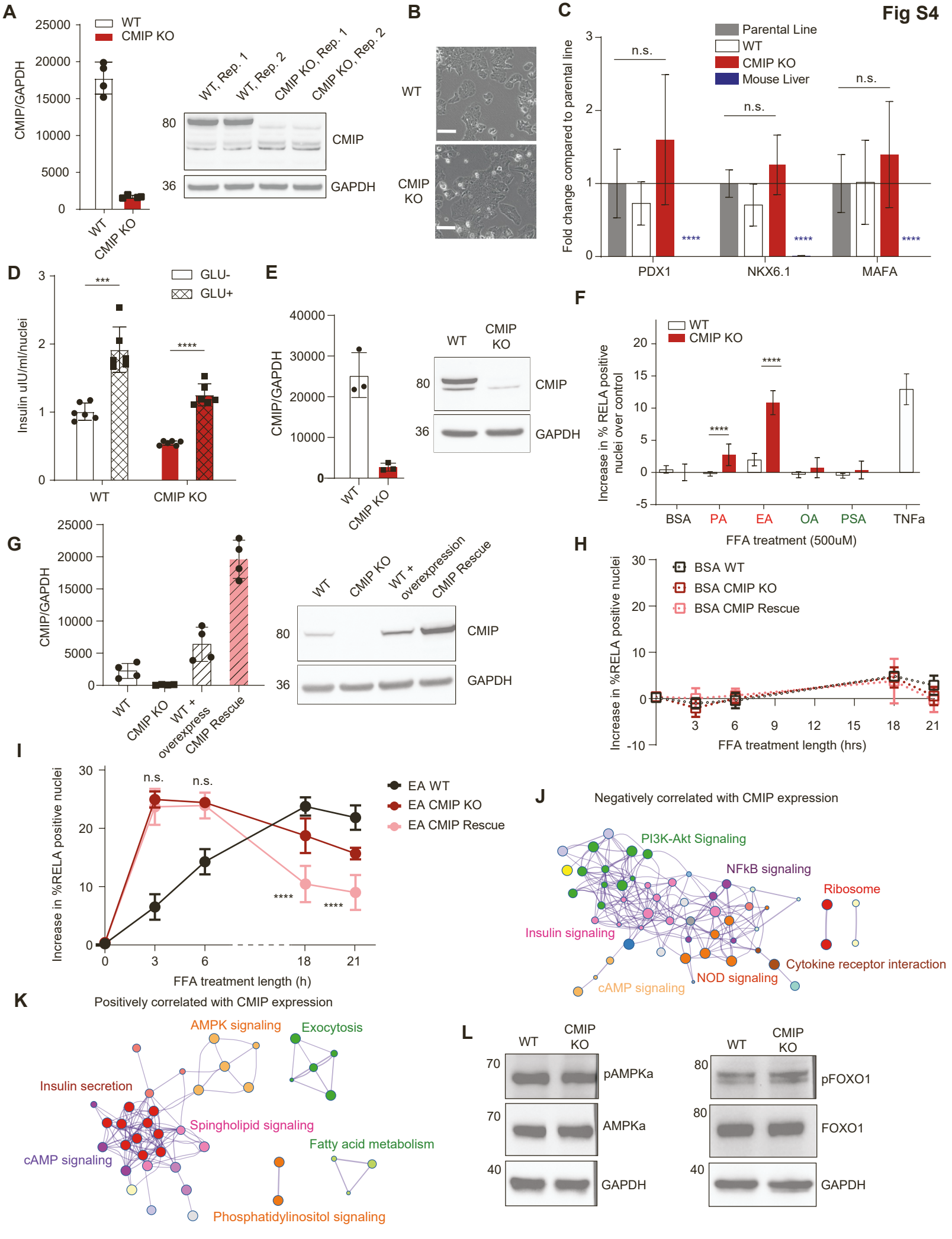
A
WT
CMIP KO
CMIP/GAPDH
25000
20000
15000
10000
5000
0
WT, Rep. 1
WT, Rep. 2
CMIP KO, Rep. 1
CMIP KO, Rep. 2
80
CMIP
36
GAPDH
B
WT
CMIP KO
C
Parental Line
WT
CMIP KO
Mouse Liver
Fold change compared to parental line
n.s.
****
PDX1
NKX6.1
MAFA
D
GLU-
GLU+
Insulin uIU/ml/nuclei
***
****
E
CMIP/GAPDH
F
Increase in % RELA positive nuclei over control
BSA
PA
EA
OA
PSA
TNFa
FFA treatment (500uM)
G
WT + overexpression
CMIP Rescue
H
BSA WT
BSA CMIP KO
BSA CMIP Rescue
Increase in %RELA positive nuclei
FFA treatment length (hrs)
I
EA WT
EA CMIP KO
EA CMIP Rescue
Increase in %RELA positive nuclei
FFA treatment length (h)
J
Negatively correlated with CMIP expression
PI3K-Akt Signaling
NFkB signaling
Ribosome
Insulin signaling
Cytokine receptor interaction
NOD signaling
cAMP signaling
K
Positively correlated with CMIP expression
AMPK signaling
Exocytosis
Insulin secretion
Spingholipid signaling
Fatty acid metabolism
cAMP signaling
Phosphatidylinositol signaling
L
pAMPKa
AMPKa
GAPDH
pFOXO1
FOXO1

Fig. S4. Beta cells are unaffected by *Cmip* deletion at baseline, related to Figure 7. (A) Quantification of CMIP protein expression in CMIP KO cells normalized to GAPDH (n = 4 blots). The primary endogenous CMIP isoform was fully deleted in the CMIP KO cells. (Right) Western blot of WT and CMIP KO lysates for CMIP and GAPDH (loading control). (B) 10x Brightfield images of WT and CMIP KO cells show no morphologic differences. Scale bars: 100 μm. (C) WT and CMIP KO cells expressed similar mRNA levels of beta cell markers compared to the parental line, and expressed significantly higher levels of PDX1, NKX6.1, and MAFA compared to the mouse liver cDNA (negative control). Two-sided ANOVA analysis, ****p < 0.0001, n = 3 replicates. (D) Insulin concentration in the supernatant of the WT and CMIP KO cells after treatment with low glucose KRB buffer (2.8 mM) or high glucose buffer (16.7 mM) for one hour each. The concentration was normalized to the number of cells present in each well. Insulin secretion doubled upon incubation with high glucose buffer for both WT and CMIP KO cells (n=6 wells). Data are mean ± SD. Multiple t-test (two-sided), ***p < 0.001, ****p < 0.0001, with Bonferroni correction. (E) Quantification of CMIP protein expression in each human iPSC-derived beta cell line normalized to GAPDH (n=3 blots). The primary endogenous CMIP isoform is fully deleted in the CMIP KO line. (Right) Western blot of WT and CMIP KO iPSC lysates for CMIP and GAPDH (loading control). (F) Percentage of cells with RELA nuclear translocation after 3 h exposure to FFAs (500 μM) or TNFα (50 ng/ml; positive control) after subtraction of baseline signal from non-treated cells. CMIP KO increased the percentage of RELA translocation after PA or EA treatment. Data are mean ± SD. Two-way ANOVA with multiple comparisons (Šídák correction, ****p < 0.0001). (G) Rescue of CMIP expression in MIN6 CMIP KO cells by overexpression of the most abundant *Cmip* isoform. Introduction of the overexpression plasmid successfully induces expression of a CMIP isoform at the appropriate molecular weight as assessed by Western blot (right). GAPDH, loading control (n=3 blots). (H) Reintroduction of CMIP into CMIP KO cells does not alter baseline NFkB activation. Percentage of cells with RELA nuclear translocation (nuclear to cytoplasmic signal > 1.2) upon treatment with BSA (500 μM) at 0, 3, 6, 18, and 21 h after subtraction of baseline signal in non-treated cells. Data are mean ± SD, n = 6-9 replicates/timepoint. No significant change with two-way ANOVA with post-hoc multiple comparisons (Bonferroni correction). (I) CMIP rescue attenuates inflammatory NFkB signaling. Percentage of cells with RELA nuclear translocation upon treatment with EA (500 μM) for the indicated times after subtraction of baseline signal from non-treated cells. Data are mean ± SD, n = 6-9 wells. Two-way ANOVA with post-hoc multiple comparisons, ****p<0.0001 with Bonferroni correction. (J,K) Network analysis of human pancreatic islet transcriptome data (GSE38642; n=51 donors) illustrating the interaction between enriched KEGG pathways from genes negatively (J) and positively (K) correlating with *CMIP* expression (FDR < 0.01). (L) CMIP KO does not alter AMPKα or FOXO1 activation. On the left is a series of Western blots for pAMPKα, AMPKα, and GAPDH (loading control) indicating no difference between the WT and CMIP KO cells (n=2 blots). On the right is a series of Western blots for pFOXO1, FOXO1, and GAPDH (loading control) indicating no difference between the WT and CMIP KO cells (n=2 blots).